MEASUREMENT OF THE ANALYZING POWERS A_y, A_{yy} OF THE H($\vec{d}, \gamma$)³He PROCESS

INAUGURALDISSERTATION

zur

Erlangung der Würde eines Doktors der Philosophie

vorgelegt der

Philosophisch-Naturwissenschaftlichen Fakultät

der Universität Basel

von

Tatiana Klechneva

aus St-Petersburg (Russland)

Basel 2004

Genehmigt von der Philosophisch-Naturwissenschaftlichen Fakultät
auf Antrag von Professor Dr. I. Sick und PD Dr. J. Jourdan.

Basel, den 10. Februar 2004

Prof. Dr. Marcel Tanner
Dekan

Acknowledgments

I would like to express my thanks to:

Abstract

The differential cross section and spin observables of the $H(\vec{d}, \gamma)^3He$ reaction can be accurately calculated starting from modern NN potentials and three nucleon forces (3NF) and using electromagnetic current operators containing in addition to the single nucleon contribution also meson exchange currents (MEC's). This opens the possibility to investigate the 3NF and MEC's effects in the polarization observables of the $\vec{d}p$-capture process. In this experiment we measure the analyzing powers A_y, A_{yy} at E_d=45 MeV and E_d=29 MeV at the extreme forward and backward angles where they are sensitive to the 3NF and MEC's effects. The experimental results are compared to the theoretical calculations done in the framework of Faddeev approach using the modern Argonne V18 NN potential with the Urbana IX 3N force. The two-body contributions in the electromagnetic current operator are included in form of explicit MEC's or using the Siegert theorem. This comparison provides additional test and information about the correctness of the 3N-system description in the framework of existing few-body theory and present nuclear dynamics.

Contents

List of Figures

List of Tables

1 Introduction

In the course of the last years new nucleon-nucleon (NN) potentials became available that describe the NN data base below the pion threshold very well. These are the Argonne V18(AV18) [1], Nijm I and Nijm II [2] and CD-Bonn [3] potentials. The binding energies of light nuclei (up to mass number A=8) calculated with these NN potentials are underestimated. Three nucleon forces (3NF) in addition to pairwise interactions are required to account for the missing binding energy [7] [6]. There are also other discrepancies between the 3N continuum experimental data and the theoretical predictions based on pure NN forces, that can be cured by adding 3NF. One example is the behavior of the elastic pd-scattering differential cross section. At the minimum of its angular distribution a systematic deviation of the calculations, based on the NN force only, from the experimental data has been reported by Koike and Ishikawa [5]. They have found that this discrepancy is observed systematically in the proton energy range from 18 MeV to 135 MeV and increases with the proton energy. That can not be explained by the incorrect treatment of Coulomb interaction only. The angular distribution of the elastic Nd-scattering cross section at higher energies has been recently investigated by Witała et al. [4] using the above mentioned modern NN potentials and Tucson-Melbourne 3NF adjusted to reproduce the ^{3}H binding energy. A large part of the discrepancy in the cross section minimum at higher energies ($E_{p\ lab} \geq 65$ MeV) can be removed by including in the 3N Hamiltonian the 3NF term V_{ijk} in addition to pairwise interactions v_{ij}:

$$\hat{H} \ = \ \sum_i \frac{\hat{\mathbf{p}}_i^2}{2\,m} + \sum_{i<j} v_{ij} + \sum_{i<j<k} V_{ijk} \qquad (1)$$

Thus, 3NF effects in few-nucleon systems are of great interest and the 3N system is the simplest one that allows us to study these effects.

The Faddeev methods [9] give a very powerful computational tool to solve the Schrödinger equation for the 3N system interacting with NN potential only. The 3NF term can also be added to the Faddeev equations. Thus the wave functions for the bound and continuum states in the $\vec{d}p$-capture process, which are important to derive the differential cross section, are exactly calculated by solving corresponding Faddeev equations [10]. That gives a possibility to estimate the contribution of the 3NF effects in the cross section and related polarization observables such as analyzing powers.

The electroweak current operator is also important for the calculation of the cross section of the H($\vec{d}, \gamma$)^{3}He reaction. It can be presented as a sum of a single-nucleon part and many-nucleon (two-, three- etc.) ones as shown in the equation (2) [9]. The leading one body part is responsible for the photon interaction with a single nucleon. The many-body currents, called also

meson exchange currents (MEC's), are due to the meson exchange mechanism of the NN interaction: two nucleons exchange mesons to which the photon can couple. It leads to the two-body contribution in the nuclear current operator. The photon can also couple to the correlated mesons what corresponds to the three-body currents, but the present calculations are restricted to the one- and two-body currents only.

$$\hat{\mathbf{j}}(\mathbf{q}) \quad = \quad \sum_i \hat{\mathbf{j}}_i^{(1)}(\mathbf{q}) + \sum_{i<j} \hat{\mathbf{j}}_{ij}^{(2)}(\mathbf{q}) + \sum_{i<j<k} \hat{\mathbf{j}}_{ijk}^{(3)}(\mathbf{q}) + \ldots \qquad (2)$$

The MEC contribution in the nuclear current operator allows us to investigate the effects of MEC's in the cross section and other spin observables. Thus, the $\vec{d}p$-capture process opens a possibility to study MEC's and 3NF effects in the 3N system in the same experiment. Deuteron energies of 29 MeV and 45 MeV were chosen because A_y for both of them was not yet measured and A_{yy} at E_d=29 MeV was measured for θ_γ=90° only. In addition, A_{yy} at the medium angles in the case of E_d=45 MeV is about 3 times less than A_{yy} at E_d=29 MeV what makes it more sensitive to the properties of the dynamical input of calculations. It is interesting to compare the ability of the theoretical calculations to describe the experimental data in these two cases.

The main aim of this experiment is to extend the precise measurements of the analyzing power A_{yy} at E_d=45 MeV to the extreme forward and backward angles and to measure A_{yy} at E_d=29 MeV as well as A_y at both deuteron energies at various angles. The experimental data should be compared with the recent theoretical calculations done by the group of J. Golak, K. Kamada, H. Wital̷a, W. Glöckle et al. [10]. These calculations were done in the framework of Faddeev approach with the Argonne V18 potential and three-nucleon interaction in form of the Urbana IX 3NF. The two-body contributions in the nuclear current operator were included in form of explicit MEC's or using the Siegert theorem. The analyzing powers A_y, A_{yy} were measured in the large region of angles with the accuracy that is enough to distinguish between different types of calculations (done using explicit MEC's or the Siegert theorem) and to be sensitive to the 3NF effects in the cases when they are present. That provides additional test of the correctness of the 3N-system description in the framework of existing few-body theory and present nuclear dynamics.

In the Chapter 2 the relation of the analyzing powers to the differential cross section is described and the reasons to study these polarization observables instead of the cross section itself are discussed. The experimental procedure and the details of the experimental setup such as gamma and recoil detectors, target, polarimeter and data taking system are described in the Chapter 3. The offline analysis of the experimental data is discussed in the Chapter 4 together with an additional background analysis procedure.

Some information about the AV18 NN potential, Urbana IX three nucleon force, the explicit MEC's and the Siegert approaches to treat the nuclear current operator is given in the Chapter 5. The experimental results are presented in the Chapter 6 in comparison with the theoretical calculations. The conclusions are discussed in the Chapter 7.

2   Vector and tensor analyzing powers A_y, A_{yy}

The vector analyzing power A_y and the tensor analyzing power A_{yy} have been chosen to be measured in the present $\vec{d}p$-capture experiment. To describe these polarization observables and their relation to the differential cross section one should define the coordinate frame.

The reaction coordinate frame used to describe the analyzing powers in the reactions which produce two particles in the final state is defined by the Madison Convention ([16]) and shown in Figure 1. Here axis Z is
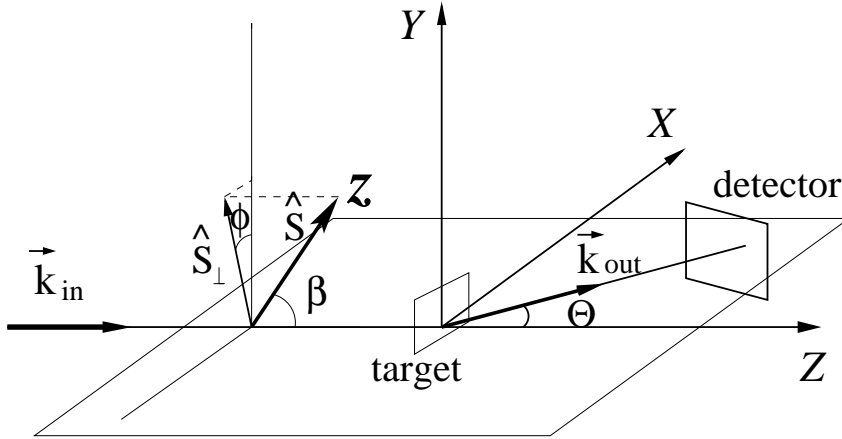
Figure 1: *The coordinate frame in which the polarization state of the incoming beam is described. Here* $\mathbf{k}_{in}$, $\mathbf{k}_{out}$ *are the momenta of the incoming and outgoing particles respectively,* $\hat{\mathbf{S}}$ *defines the spin state of the incoming beam and* $\mathcal{Z}$ *is its quantization axis.*

taken along the momentum of the incoming beam $\mathbf{k}_{in}$, axis Y is taken along $\mathbf{k}_{in} \times \mathbf{k}_{out}$ where $\mathbf{k}_{out}$ is the momentum of the outgoing particles and axis X is taken to form a right-handed coordinate system. The beam polarization axis $\mathcal{Z}$ is defined in this coordinate system by two angles: by the angle β which $\mathcal{Z}$ makes with the axis Z and by the angle Φ between axis Y and projection of the vector $\mathbf{S}$ on the plain (XY), where $\hat{\mathbf{S}}$ is the deuteron spin operator. In this $\vec{d}p$-capture experiment the polarization axis of the deuteron beam was chosen to be parallel to the axis Y, so $\beta = 90^o$ and $\Phi = 0^o$. The advantages of this choice are discussed below.

Since the deuteron beam is symmetric about the spin quantization axis $\mathcal{Z}$, a polarization state in the beam coordinate frame is described by the following vector and tensor polarization numbers:

$$P_{\mathcal{Z}} = N_+ - N_-, \qquad\qquad P_{\mathcal{X}} = 0, \qquad\qquad P_{\mathcal{Y}} = 0,$$

$$P_{\mathcal{Z}\mathcal{Z}} = 1 - 3N_0, \qquad\qquad P_{\mathcal{X}\mathcal{X}} = P_{\mathcal{Y}\mathcal{Y}} = -\frac{1}{2}(1 - 3N_0),$$

$$P_{\mathcal{X}\mathcal{Y}} = P_{\mathcal{Y}\mathcal{Z}} = P_{\mathcal{X}\mathcal{Z}} = 0. \qquad (3)$$

Here N_+, N_-, N_0 are the fractional populations of deuterons with the spin $\mathcal{Z}$-projections $m_I= +1, -1, 0$; $N_+ + N_- + N_0 = 1$. In the above mentioned reaction coordinate frame the beam polarization components are defined [17] as :

$$P_x = -sin(\beta)sin(\Phi)P_{\mathcal{Z}},$$
$$P_y = sin(\beta)cos(\Phi)P_{\mathcal{Z}},$$
$$P_z = cos(\beta)P_{\mathcal{Z}} \qquad (4)$$

and

$$P_{xy} = -\frac{3}{2}sin^2(\beta)cos(\Phi)sin(\Phi)P_{\mathcal{Z}\mathcal{Z}},$$
$$P_{yz} = \frac{3}{2}sin(\beta)cos(\beta)cos(\Phi)P_{\mathcal{Z}\mathcal{Z}},$$
$$P_{xz} = -\frac{3}{2}sin(\beta)cos(\beta)sin(\Phi)P_{\mathcal{Z}\mathcal{Z}},$$
$$P_{xx} = \frac{1}{2}(3sin^2(\beta)sin^2(\Phi) - 1)P_{\mathcal{Z}\mathcal{Z}},$$
$$P_{yy} = \frac{1}{2}(3sin^2(\beta)cos^2(\Phi) - 1)P_{\mathcal{Z}\mathcal{Z}},$$
$$P_{zz} = \frac{1}{2}(3cos^2(\beta) - 1)P_{\mathcal{Z}\mathcal{Z}}. \qquad (5)$$

The differential cross section of the $\vec{d}p$-capture process for a polarized deuteron (deuteron which has a specific magnetic quantum number) is defined as [10]

$$\frac{d\sigma_{cm}}{d\Omega} \sim \sum_{M_p, M_{3He}} \sum_{\lambda=\pm 1} |J^\lambda_{M_p M_d M_{3He}}(\mathbf{p}, \mathbf{q})|, \qquad (6)$$

where

$$J^\lambda_{M_p M_d M_{3He}}(\mathbf{p}, \mathbf{q}) = \langle \Psi_{3He}(\mathbf{p}')|\hat{\mathbf{e}}^*_\lambda(\mathbf{q}) \cdot \hat{\mathbf{j}}^\dagger(\mathbf{q})|\Psi^{(+)}_{dp}(\mathbf{p})\rangle. \qquad (7)$$

Here $\mathbf{q}$ is the photon momentum, $\hat{\mathbf{e}}_\lambda(\mathbf{q})$ ($\lambda = \pm 1$) is the spherical component of the photon polarization vector, $\mathbf{p}$ and $\mathbf{p}'$ are the momenta before and after photon emission, M_i (i=d, p, ^{3}He) are the magnetic quantum numbers of deuteron, proton and ^{3}He. The differential cross section given in expression (6) can be expanded in terms of spherical tensors:

$$\frac{d\sigma_{cm}}{d\Omega} = \sum_{kq}(-1)^q \tau_{kq} A_{kq}(\theta_{cm}) \qquad (8)$$

Here k and q vary from 0 to 2, τ_{kq} is related to the polarization density matrix elements and $A_{kq}(\theta_{cm})$ is related to the transition matrix elements, θ_{cm} describes the angle between incoming deuterons and outgoing photons in the center of mass system. The unpolarized cross section can be defined as

$$\frac{d\sigma_0}{d\Omega} \quad = \quad \frac{1}{3}A_{00}(\theta_{cm}),$$

other terms can be presented as

$$T_{kq}(\theta_{cm}) \quad = \quad A_{kq}(\theta_{cm})/A_{00}(\theta_{cm}).$$

The differential cross section can then be written as

$$\frac{d\sigma_{cm}}{d\Omega} \quad = \quad \frac{d\sigma_0}{d\Omega}[1 + \sum_{kq,k>0} (-1)^q \tau_{kq}T_{kq}(\theta_{cm}], \tag{9}$$

where $T_{kq}(\theta_{cm})$ are the spherical analyzing power tensor components. Thus, an analyzing power tensor component defines quantitatively the contribution of the corresponding deuteron polarization component in the total differential cross section. The expression for the differential cross section, given in the center of mass frame by equation (9), can be written in the reaction coordinate frame using the relationships between spherical and Cartesian analyzing power tensor components as [17], [18]:

$$\begin{aligned}
\frac{d\sigma(\Phi,\theta,\beta)}{d\Omega} \quad &= \quad \frac{d\sigma_0(\theta)}{d\Omega}[1 + \frac{3}{2}(P_x A_x(\theta) + P_y A_y(\theta) + P_z A_z(\theta)) \\
&+ \quad \frac{2}{3}(P_{xy}A_{xy}(\theta) + P_{yz}A_{yz}(\theta) + P_{xz}A_{xz}(\theta)) \\
&+ \quad \frac{1}{3}(P_{xx}A_{xx}(\theta) + P_{yy}A_{yy}(\theta) + P_{zz}A_{zz}(\theta))], \tag{10}
\end{aligned}$$

where $\frac{d\sigma_0(\theta)}{d\Omega}$ is the unpolarized cross section, θ is the angle between incoming deuterons and outgoing photons, P_i, P_{ij} are the Cartesian components of the beam vector and tensor polarization (see equations (4) and (5)), A_i and A_{ij} are the analyzing power functions. Taking into account the fact that in this experiment $\beta = 90^o$ and $\Phi = 0^o$ one can express the differential cross section from the equation (10) in terms of $P_{\mathcal{Z}}$ and $P_{\mathcal{ZZ}}$ as:

$$\frac{d\sigma(\theta)}{d\Omega} \quad = \quad \frac{d\sigma_0(\theta)}{d\Omega}[1 + \frac{3}{2}P_{\mathcal{Z}}A_y(\theta) + \frac{1}{2}P_{\mathcal{ZZ}}A_{yy}(\theta)] \tag{11}$$

The choice $\beta = 90^o$ and $\Phi = 0^o$ allows us to expose A_y, A_{yy} in the simplest possible way what gives a possibility to measure both of them in the same experiment.

The analyzing powers A_y, A_{yy} were chosen to be measured because they

are sensitive to the $S-D$ transition amplitudes which are related to the non-nucleonic degrees of freedom, whereas the dominated contribution in the unpolarized cross section is done by the $S-S$ transitions. The MEC's effects are especially large at the extreme forward and backward angles as shown in Figures 2 and 3. In these Figures A_y, A_{yy} as functions of the scattering angle θ_{cm} at $E_d =29$ MeV and $E_d =45$ MeV calculated using explicit MEC's or the Siegert theorem are presented. One can also compare the calculations done including and excluding 3NF. The differential cross section as a function of the scattering angle θ_{cm} at $E_d =29$ MeV and $E_d =45$ MeV calculated using explicit MEC's or the Siegert theorem including and excluding 3NF is presented in Figure 4. Whereas the behavior of the analyzing powers is highly dependent on the MEC's effects, the cross section is not sensitive to the type of calculations. The 3NF effects are much less distinct, for A_y and $d\sigma/d\Omega$ at $E_d=45$ MeV they are negligible.
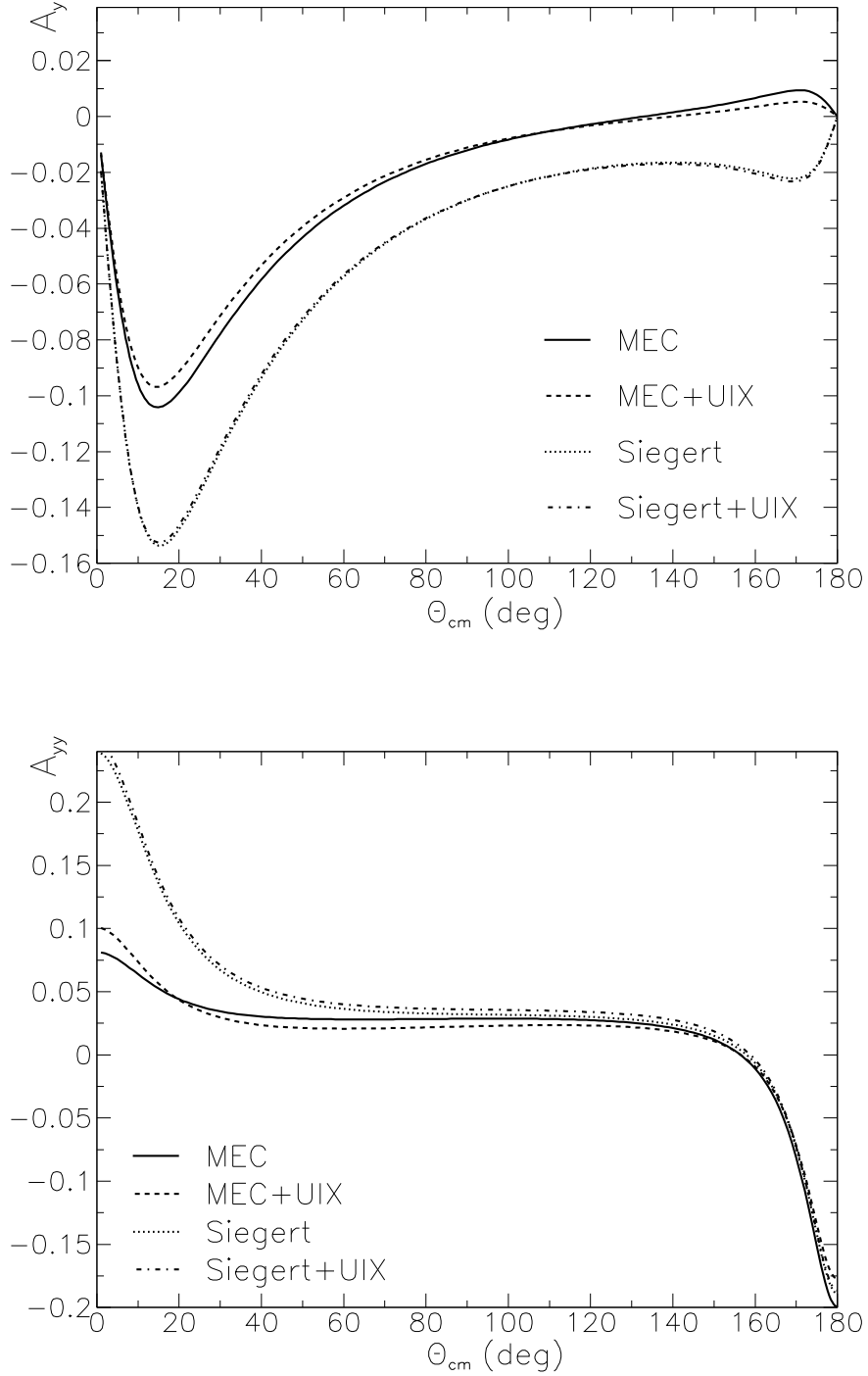
Figure 2: *A_y, A_{yy} at E_d=29 MeV as functions of the c.m. scattering angle calculated using explicit MEC's and the Siegert theorem including and excluding Urbana IX 3NF (see section 5).*
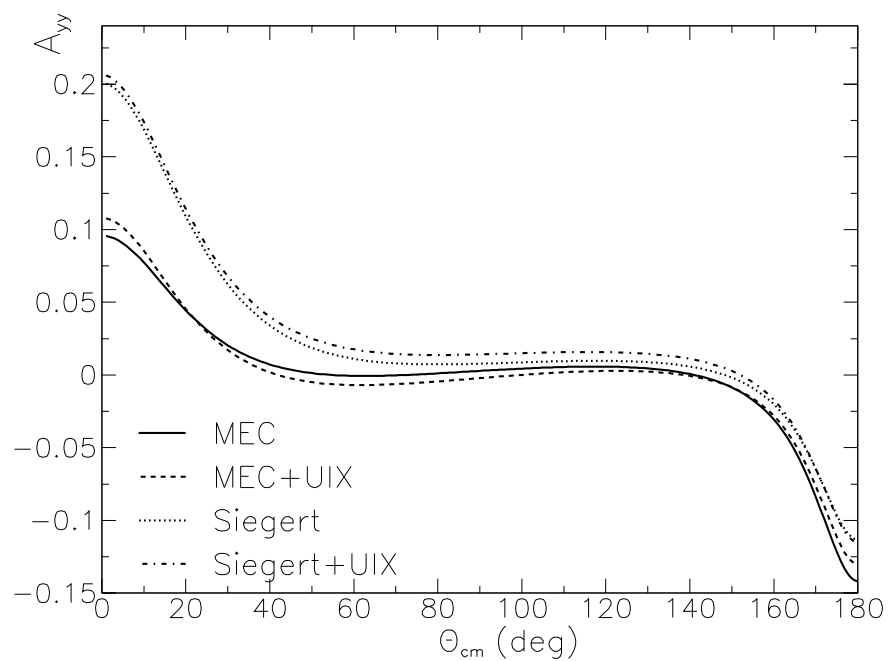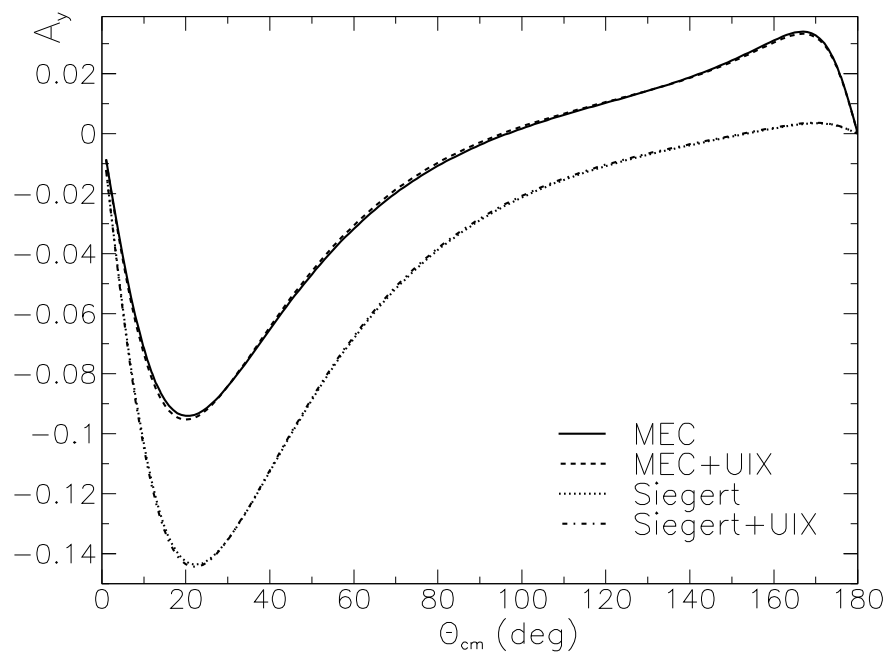
Figure 3: A_y, A_{yy} at E_d=45 MeV as functions of the c.m. scattering angle calculated using explicit MEC's and the Siegert theorem including and excluding Urbana IX 3NF(see section 5).
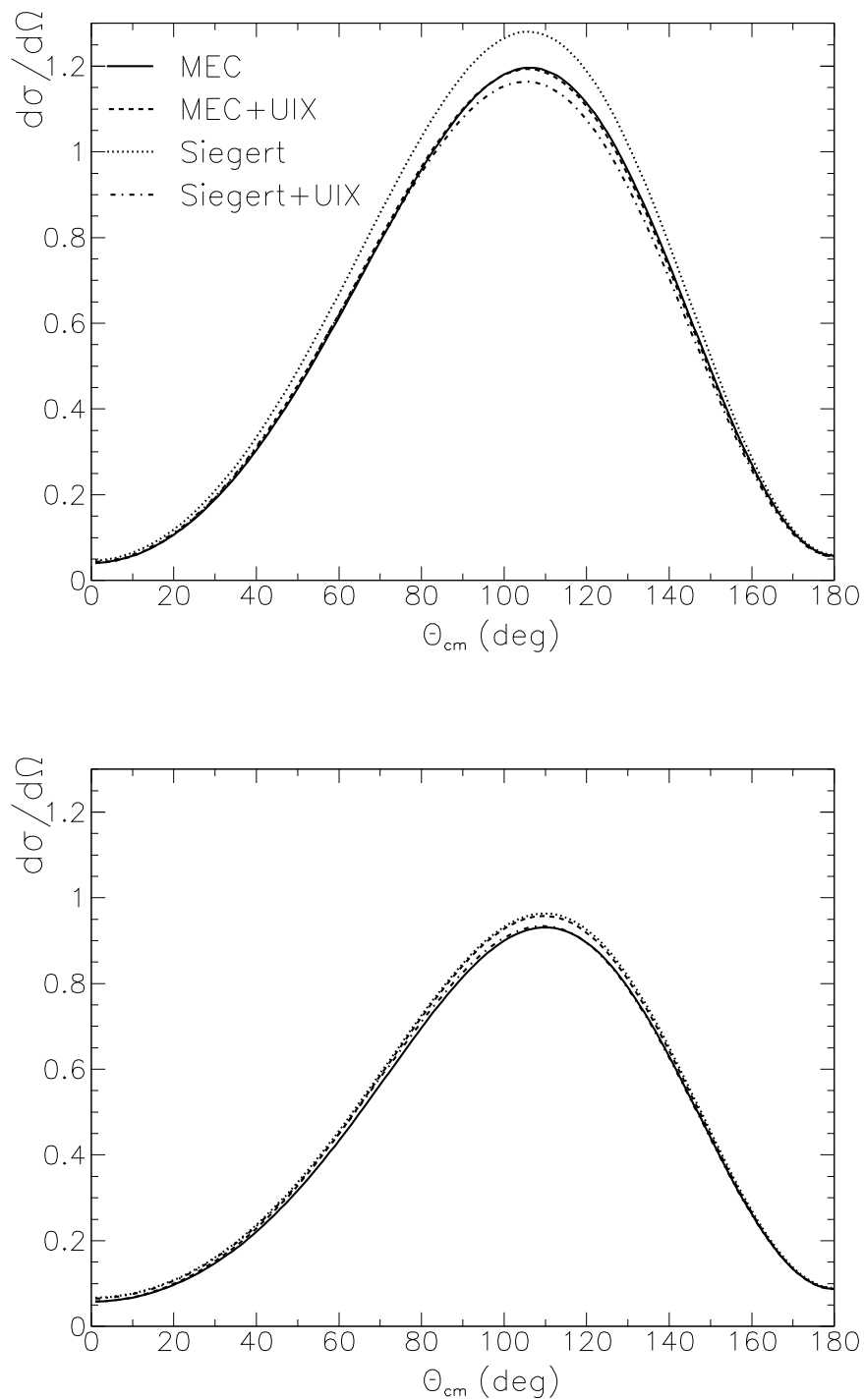
Figure 4: $d\sigma_0/d\Omega$ at $E_d=29$ MeV (upper plot) and $E_d=45$ MeV (lower plot) as a function of the c.m. scattering angle θ_{cm} calculated using explicit MEC's including and excluding Urbana IX 3NF and using the Siegert theorem also including and excluding Urbana IX 3NF.

3   Experiment

The $\vec{d}p$-capture experiment took place in August and October 2000 at the Paul Scherrer Institute (PSI) in Villigen. A polarized deuteron beam at deuteron energies of 45 MeV and 29 MeV was provided by the Philips cyclotron and its polarized ion source [21]. The task of the experiment was to detect gammas produced in the reaction $\vec{d} + \mathrm{H} \rightarrow \gamma + {}^3\mathrm{He}$ in coincidence with the recoil particles ${}^3\mathrm{He}$. It allowed us to identify the capture-events despite the low cross section ($0.1 \div 1 \ \mu b$) of this process at energies of several tens of MeV and then to extract A_y, A_{yy} from the difference between γ-counts obtained for different deuteron polarizations.

The schematic view of the experimental setup is shown in Figure 5. The
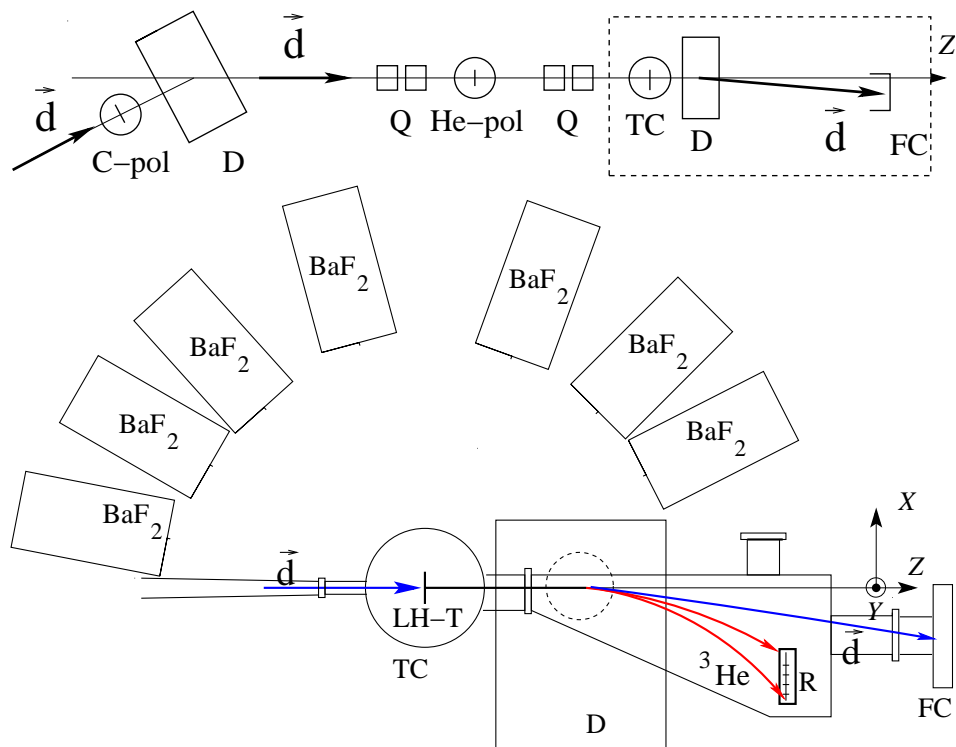
Figure 5: *Schematic overview of the beam line in the experimental hall NE-C at PSI and of the experimental setup. Here C-pol - carbon polarimeter, Q - quadrupole doublet, He-pol - ${}^4He$-polarimeter, TC - target chamber, LH-T - liquid hydrogen target, D - dipole magnet to separate ${}^3He$ and unscattered deuterons, R - recoil-detectors, FC - Faraday cup.*

polarized deuteron beam from the accelerator passed first through the carbon polarimeter chamber, where a CsI scintillation detector was placed at 30° below the beam axis to control the beam time structure. Deuterons were scattered from a thin carbon foil and the distribution of their time

of flight relative to the radio-frequency (RF) signal from the cyclotron was measured. Then the beam went through the "Basler Chamber" where the ^{4}He-polarimeter for the absolute polarization measurements was installed. Then the beam passed the scattering chamber where deuterons interacted with the liquid hydrogen target. The target chamber was directly connected with the transport vacuum chamber, developed and built especially for this experiment to transport the recoil particles and unscattered deuterons. In order to separate them from each other a dipole magnet downstream to the target chamber was installed. To detect the deflected recoil particles with energies of $17 \div 21$ MeV for $E_d = 29$ MeV and $26 \div 31$ for $E_d = 45$ MeV, the detectors on the base of the plastic scintillator *Pilot U* were used. The inorganic scintillator BaF_2 was chosen to detect gammas with energies of $13 \div 16$ MeV for $E_d = 29$ MeV and $17 \div 24$ MeV for $E_d = 45$ MeV. There were four detector boxes which were installed at the chosen laboratory γ-angles from 27° to 169°. The unscattered deflected deuteron beam was stopped in the Faraday cup. The details of some experimental devices are given below.

3.1   Polarized deuteron beam

As it was mentioned in section 2, the incoming deuteron beam is characterized by the vector polarization P_Z and the tensor polarization P_{ZZ}. To have P_Z, $P_{ZZ} \neq 0$ (see equations (3)) one should obtain different populations of $m_I = +1, -1, 0$ states, what is possible by using the Zeeman effect of the D-atom hyperfine structure in an external magnetic field. The schematic energy level diagram of the D-atom in an external magnetic field is shown in Figure 6. At zero external magnetic field six possible energy levels are degenerate; when the external field is on, they become resolved. Energy in this diagram is measured in zero-field splitting units, the strength of the external magnetic field is measured in critical-field units, the external field B is "strong" when $B/B_c \gg 1$ and "weak" when $B/B_c \leq 1$. The D-atoms with $m_j = +1/2$ $(-1/2)$ can be easily separated from each other by focusing (defocusing) in the inhomogeneous magnetic field, but this produces an atomic polarization only and the populations of the states with different m_I are still equal. To obtain nuclear polarization the adiabatic passage method is used [19]. The adiabatic passage method can be applied to the weak field (WF) region where F is still a good quantum number and to the strong field (SF) region where it is not true any more. The WF RF-transitions cause the interchange of the populations of states m_F and $-m_F$. In terms of the energy level diagram it causes the transitions $1 \leftrightarrow 4, 2 \leftrightarrow 3, 5 \leftrightarrow 6$. The SF RF-transition causes the interchange of two chosen level populations only. In our case two different strong field transitions were involved to interchange the populations of the states $3 \leftrightarrow 5$ (SF1) and $2 \leftrightarrow 3$ (SF2). Thus, the values of the vector and tensor polarization

were varied by combining WF, SF1 and SF2 transitions and by focusing only the $m_j=+1/2$ part of the D-atom beam.

The atoms were then ionized maintaining the nuclear polarization. Po-
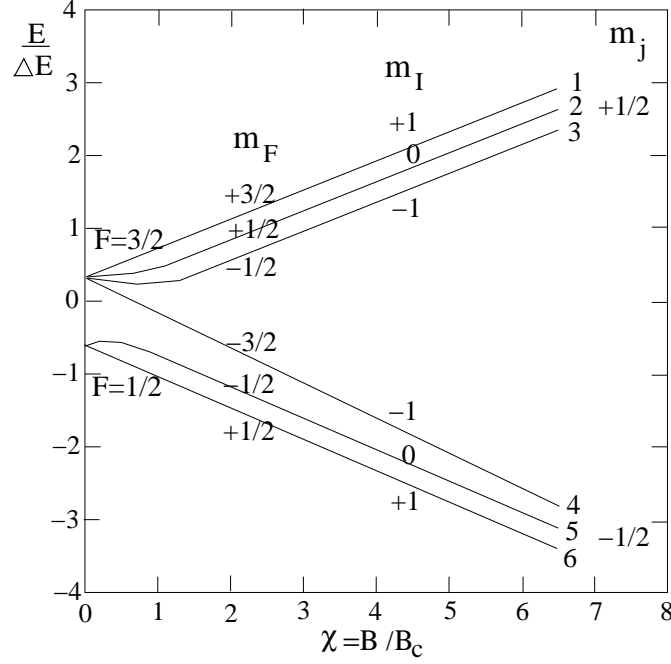
Figure 6: *Energy level diagram of the D-atom in an external magnetic field.* ΔE *is the zero field energy level splitting,* $B_c = (g_I - g_j)\mu_B/\Delta E$.

larization modes used in this experiment are given in Table 1 together with corresponding nominal polarization values. The polarization state was changed every 3 seconds in the following way: a → d → b → e → c.

Pol. state	SF2	SF1	WF	P_z	P_{zz}
a	off	off	off	0	0
b	on	off	off	+1/3	+1
c	off	on	off	+1/3	−1
d	on	off	on	−1/3	−1
e	off	on	on	−1/3	+1

Table 1: *Polarized beam source modes and nominal polarization values.*

3.2   Polarimetry

To measure the absolute deuteron beam polarization values, the reaction of the elastic $\vec{d}\,^4$He-scattering was used. Deuterons were elastically scattered from ^{4}He in the target cell (containing helium at a pressure of 0.5 bar) installed in the "Basler Chamber". The recoil ^{4}He were detected at $\theta_{^4He\ lab} = \pm 15^o$ using two 700 μm thick (500 μm for $E_d = 29$ MeV) passivated implanted planar silicon detectors (PIPS) chosen due to their very good energy resolution crucial for these measurements. Before entering the PIPS detectors, the recoil ^{4}He passed a collimator system consisting of one Ta-collimator at a distance of 12 cm from the center of the cell and one Ta-collimator directly in front of the detector at a distance of 45 cm from the center of the cell. This limited the horizontal acceptance of the detectors to $\sim 1^o$ and shielded them from the particles scattered from the cell window. Elastically scattered deuterons were discriminated due to the low deposited energy.

The energy spectra of scattered ^{4}He at $\theta_{^4He\ lab} = 15^o$ for $E_d = 29$ MeV and $E_d = 45$ MeV are shown in Figure 7. The area between two vertical lines was used for the analysis.

The laboratory scattering angles $\pm 15^o$ were chosen because they corre-
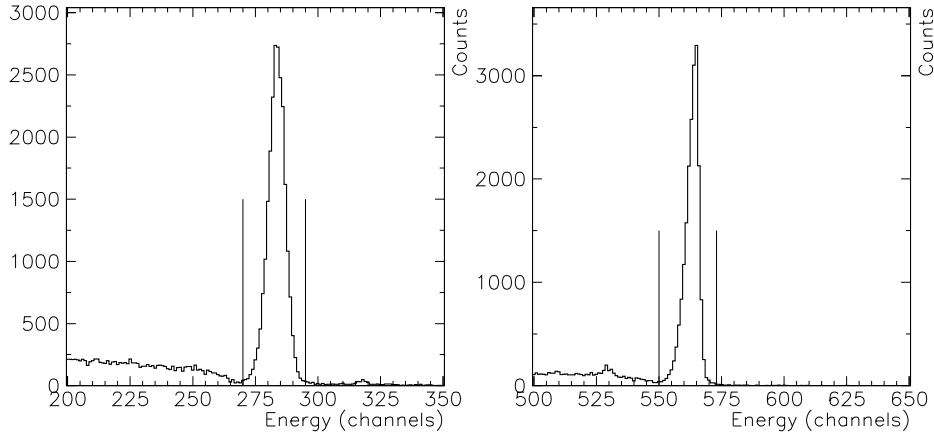
Figure 7: ^{4}He-energy spectra at $\theta_{^4He\ lab} = 15^o$, $E_d = 29$ MeV (left) and $E_d = 45$ MeV (right). The integration limits are shown as vertical lines.

spond to the center of mass scattering angle of 150°, where A_y, A_{yy} of this reaction are maximal [23], [24]:

$A_{yy} = 0.921 \pm 0.013$, $A_y = 0.497 \pm 0.011$ at E_d=45 MeV,

$A_{yy} = 0.910 \pm 0.016$, $A_y = 0.846 \pm 0.02$ at E_d=29 MeV.

The polarization of the deuteron beam was extracted using equation (11)
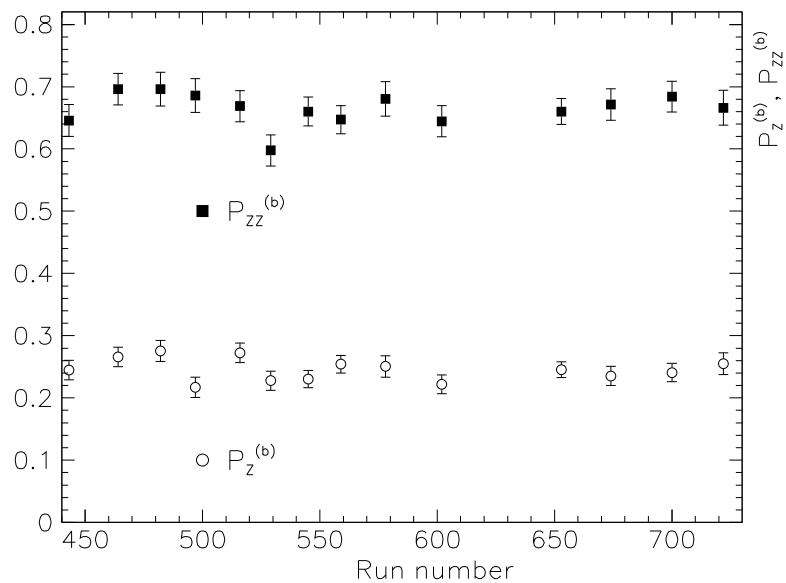
Figure 8: $P_{\mathcal{Z}}^{(b)}$, $P_{\mathcal{Z}\mathcal{Z}}^{(b)}$ measured using the ^4He-polarimeter during the first part of the experiment.
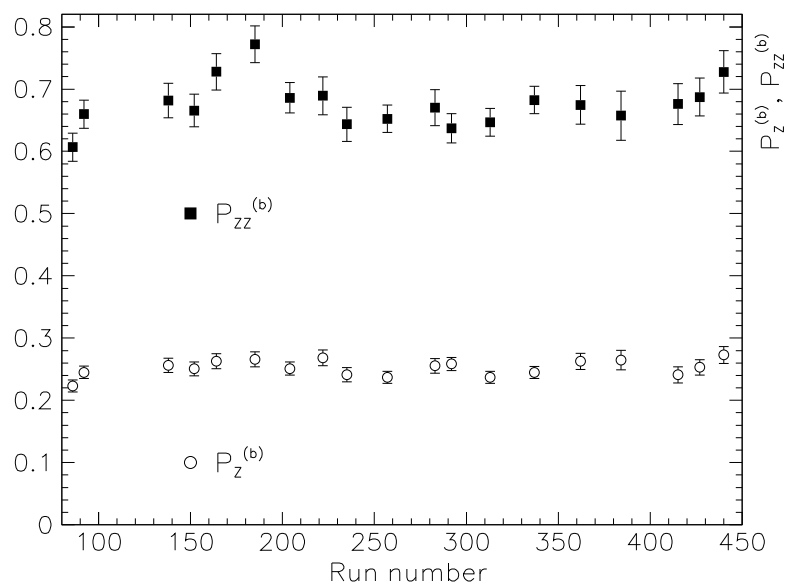
Figure 9: $P_{\mathcal{Z}}^{(b)}$, $P_{\mathcal{Z}\mathcal{Z}}^{(b)}$ measured using the ^4He-polarimeter during the second part of the experiment.

and the fact that the differential cross section is proportional to the number of events counted by the detector. The following equations can be written for each polarization state i:

$$K_+^i N_+^i = N_+^0 (1 + \frac{3}{2} P_{\mathcal{Z}}^i A_y + \frac{1}{2} P_{\mathcal{Z}\mathcal{Z}}^i A_y),$$

$$K_-^i N_-^i = N_-^0 (1 - \frac{3}{2} P_{\mathcal{Z}}^i A_y + \frac{1}{2} P_{\mathcal{Z}\mathcal{Z}}^i A_y). \tag{12}$$

Here N_+^i (N_-^i) are the number of events detected by the left (right) detector, K_+^i (K_-^i) is the dead time (DT) and Faraday cup (FC) correction coefficient:

$$K_{+(-)}^i = \frac{FC_{+(-)}^0}{FC_{+(-)}^i} \frac{(1 - DT_{+(-)}^0)}{(1 - DT_{+(-)}^i)}.$$

From the equations (12) one determines the expressions for $P_{\mathcal{Z}}^i$, $P_{\mathcal{Z}\mathcal{Z}}^i$:

$$P_{\mathcal{Z}\mathcal{Z}}^i = (\frac{K_+^i N_+^i - N_+^0}{N_+^0} + \frac{K_-^i N_-^i - N_-^0}{N_-^0}) \frac{1}{A_{yy}}$$

$$P_{\mathcal{Z}}^i = (\frac{K_+^i N_+^i - N_+^0}{N_+^0} - \frac{K_-^i N_-^i - N_-^0}{N_-^0}) \frac{1}{3 A_y} \tag{13}$$

The expressions for errors were derived from the equations (13) using

Polarization	E_d=45 MeV		E_d=29 MeV	
$P_{\mathcal{Z}}^b$ $\Delta P_{\mathcal{Z}}^b$	0.2447	0.0084	0.2482	0.0085
$P_{\mathcal{Z}}^c$ $\Delta P_{\mathcal{Z}}^c$	0.2167	0.0072	0.2277	0.0077
$P_{\mathcal{Z}}^d$ $\Delta P_{\mathcal{Z}}^d$	-0.2545	0.0083	-0.2583	0.0087
$P_{\mathcal{Z}}^e$ $\Delta P_{\mathcal{Z}}^e$	-0.2808	0.0094	-0.2720	0.0092
$P_{\mathcal{Z}\mathcal{Z}}^b$ $\Delta P_{\mathcal{Z}\mathcal{Z}}^b$	0.6569	0.0141	0.6725	0.0173
$P_{\mathcal{Z}\mathcal{Z}}^c$ $\Delta P_{\mathcal{Z}\mathcal{Z}}^c$	-0.6017	0.0124	-0.6582	0.0166
$P_{\mathcal{Z}\mathcal{Z}}^d$ $\Delta P_{\mathcal{Z}\mathcal{Z}}^d$	-0.6076	0.0125	-0.6435	0.0163
$P_{\mathcal{Z}\mathcal{Z}}^e$ $\Delta P_{\mathcal{Z}\mathcal{Z}}^e$	0.5608	0.0123	0.6700	0.0172

Table 2: *Mean polarization values for the first part of the experiment (E_d=45 MeV) and for the second part of the experiment (E_d=29 MeV).*

[22]. It should be pointed out that not only the statistical errors due to $\Delta N_{+(-)}^i$ but also the systematical ones due to the uncertainties in A_y, A_{yy} coming into the expressions (13) were included in the polarization errors. The polarization of the deuteron beam was measured every 8 hours. In Figures 8 and 9 examples of the behavior of the deuteron-beam polarization

during the first (E_d =45 MeV) and the second (E_d =29 MeV) part of the experiment are shown. The mean polarization values calculated with all polarization runs and used in the data analysis together with their errors are given in Table 2.

3.3 γ-detectors

As it was mentioned above, the γ-detectors for this experiment were built on the base of the inorganic scintillator BaF_2. The light pulse of this scintillator has a short and a long component. They are characterized by a decay time of 0.7 ns and 620 ns and a light emission spectrum maximum at 220 nm and 310 nm respectively [26]. The BaF_2 fast component with its excellent time characteristics allows us to resolve gammas and neutrons and to reject the background more effectively than with any other scintillator. In addition, BaF_2 has a very good efficiency for γ-ray detection due to a high density of 4.89 g/cm^3 and a good energy resolution of about 16% (short component) at $E_\gamma \approx$ 20 MeV for big 8×8×25 cm^3 crystals. The production of BaF_2 crystals of this size is very difficult, but this problem was succcessfully solved by the State Optical Institute in St-Petersburg (Russia).
Four aluminium detector boxes with a wall-thickness of 5 mm were used, each of them contained four crystals. These were connected using the special optical gel transparent for the UV radiation (*Baysilone Öl* M 600000 by GE Bayer Silicons GmbH) with the fast photomultiplier tubes Philips XP4318B. The schematic view of the detector box is presented in Figure 10. The light emission diode (LED) was mounted into the back side of each detector box. It was operated with the special LED-Pulser with a frequency of ∼ 10 Hz. The LED response signal of each crystal was used for the electronics tuning. In the offline-analysis the LED signals were used to adjust the main signal amplitude due to HV-drift or other significant fluctuations. The detector boxes were installed at a distance of ∼ 80 cm from the center of the target. They were quite close to the magnet, especially at the forward angles (see Figure 5). In order to protect the photomultiplier tubes from a magnetic field of about 50 G, a cilindrical μ-metal shielding with a wall-thickness of 1 mm around each tube was used as shown in Figure 10. For better protection of two detectors at the very forward angles two closed μ-metal boxes for the whole detector with a wall-thickness of 1.5 mm were used. The lead shielding with a thickness of 5 cm on the sides and the top and 2.5 cm on the bottom of the detector boxes protected the detectors from the undesirable radiation.
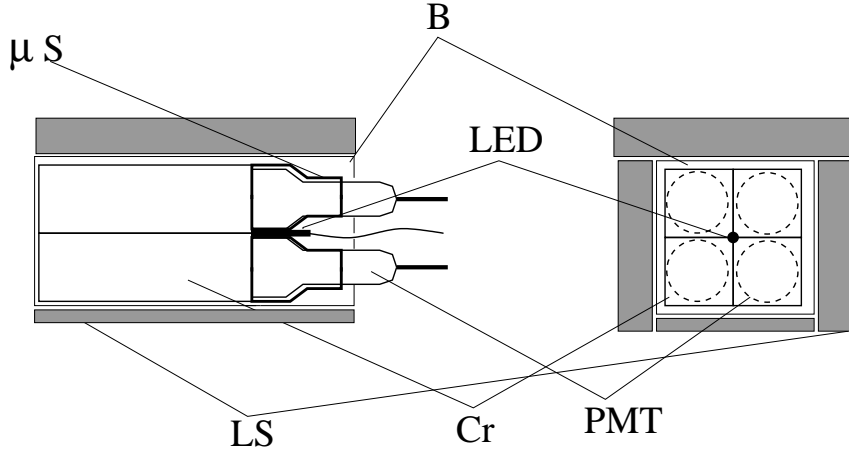
Figure 10: *Schematic view of the γ-detector. Symbols denote: B - detector box, Cr - BaF$_2$ crystals, PMT - photomutiplier tubes, μS - μ-metal shielding around each photomultiplier tube, LS - lead shielding around the detector box, LED - light emission diode.*

3.4   Recoil-detectors

The recoil-detectors were built on the base of the organic scintillator *Pilot U* with a thickness of 1.2 mm. They detected deflected in a magnetic field ^{3}He nuclei, recoiling in a cone between 0.4^o and 2.6^o for both deuteron energies. The strength of the magnetic field (0.640 T for E_d =45 MeV and 0.430 T for E_d =29 MeV at the center of the dipole) was chosen to deflect the initial deuteron beam by $\sim$ 8° what allowed us to separate ^{3}He and deuterons by more than 10°.

The position and size of the recoil detector as well as the construction parametes of the specially built transport chamber (see Figure 11) were defined by simulations of deuteron and ^{3}He trajectories in a magnetic field. These simulations were done using the *Fortran*-code "raytrace" [25] and the real magnetic field map measured at PSI. The angular and spacial deviations of particles, leaving the target, from their scattering direction were determined by the beam divergence and size in front of the target (less than 6 mr and 0.5 cm) and the multiple scattering in the target. They were randomized using two gaussian distributions with given σ's. The full acceptance of the recoil detectors was chosen to capture 99% of the incoming particles. The size of *Pilot U*-pieces was chosen to have nearly equal ^{3}He fluxes in all detectors to protect the electronics from the over-load.

The photomultipliers were mounted outside of the transport chamber at a distance of about 50 cm to protect them from the magnetic field. They were connected with the detectors using the light guides within the aluminium tubes as it is shown in Figure 11.
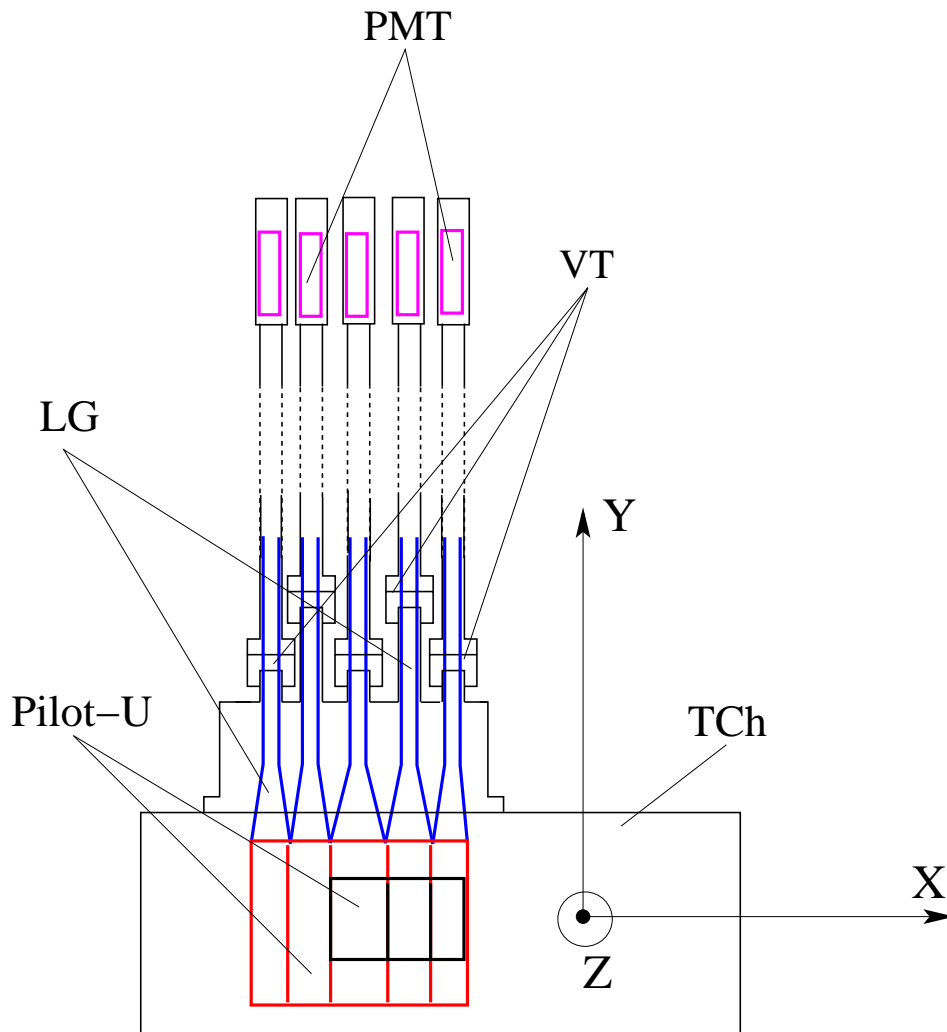
Figure 11: *Schematic view of the recoil detectors. Symbols denote: TCh - transport chamber, PMT - photomutiplier tubes, LG - light guides, VT - vacuum tight connections. The position and size of the Pilot U-pieces are shown with the black lines for E_d=45 MeV and with the red lines for E_d=29 MeV.*

3.5   Target

The liquid hydrogen target was installed in the aluminium target chamber. It had a diameter of 36 cm and a wall-thickness of 3 mm. The target chamber was designed to correspond to the experimental conditions: the standard backward flange was replaced by a special telescopic one (see Figure 5) what made possible measurements at the very backward angle. The target had a thickness of 14 mg/cm^2 and was operated at a temperature of ≤ 16 K and a pressure of ~ 0.28 Bar. The target was chosen to be as thin as possible to reduce the ^{3}He energy losses and multiple scattering. The pressure was chosen to be low enough to use the *havar* target windows with a thickness of 2.5 μm only. It reduced the multiple scattering of ^{3}He. The target was cooled by a reservoir of liquid hydrogen at a temperature of 10 K mounted on the top of it. The liquid hydrogen was cooled down with a closed-cycle helium refrigerator (more details are given in [20]).

3.6   Electronics and Data taking

The schematic setup of the electronics is shown in Figure 12. The main features of the electronics are:

- The signals from the recoil detectors and all crystals of each BaF$_2$-detector passed the 50 Hz filter.

- The signals from the BaF$_2$-detectors were multiplexed. One part provided the information about the amplitude of the long component signal (ADC L), another one was clipped and used for timing. It also gave the information about the amplitude of the short component signal (ADC S).

- Constant Fraction Discriminator was used for the amplitude-independent timing.

- The signals fed into the Analog Digital Converter (ADC) and Time Digital converter (TDC) were delayed to synchronize them with the gates or start signals.

- The ADC L, ADC S and ADC Recoil (ADC R) integrated the signals over the following gate-widths:
  ADC L $-$ 700 ns,
  ADC S $-$ 25 ns,
  ADC R $-$ 40 ns.

- TDC C's recorded the information about coincidences between given recoil and given BaF$_2$-detector. They started with a signal from any BaF$_2$-detector, it has a width of 25 ns. The use of the coincidence-technique allowed us to reduce the number of counted background events, what led to the decrease of the electronics dead time.

- The RF-signal from the cyclotron was used to reduce the number of accidental coincidences which were not correlated with the coming beam bunch.

- A signal from the Faraday cup, a real-time clock and pulser signals as well as the current polarization state signal were fed into scalers.

- The pulser signal passed the polarimeter electronic tract parallel to the real signals from the solid state detectors and was fed into both (left and right) polarization spectra.

- The dead time of the data acquisition system was determined by the ratio of the number of "pretrigger" events (the total number of coincidences between BaF_2 and recoil detectors) to the number of "trigger" events (the number of unvetoed coincidences) in the scalers. The dead time of the polarimeter was defined for left and right detector separately by the ratio of the number of pulser events counted in left and right polarization spectrum respectively to the total number of pulser events read from the scaler.

- As long as the signal "run started" was set, the ADC and TDC modules and scalers were read from the front-end computer.
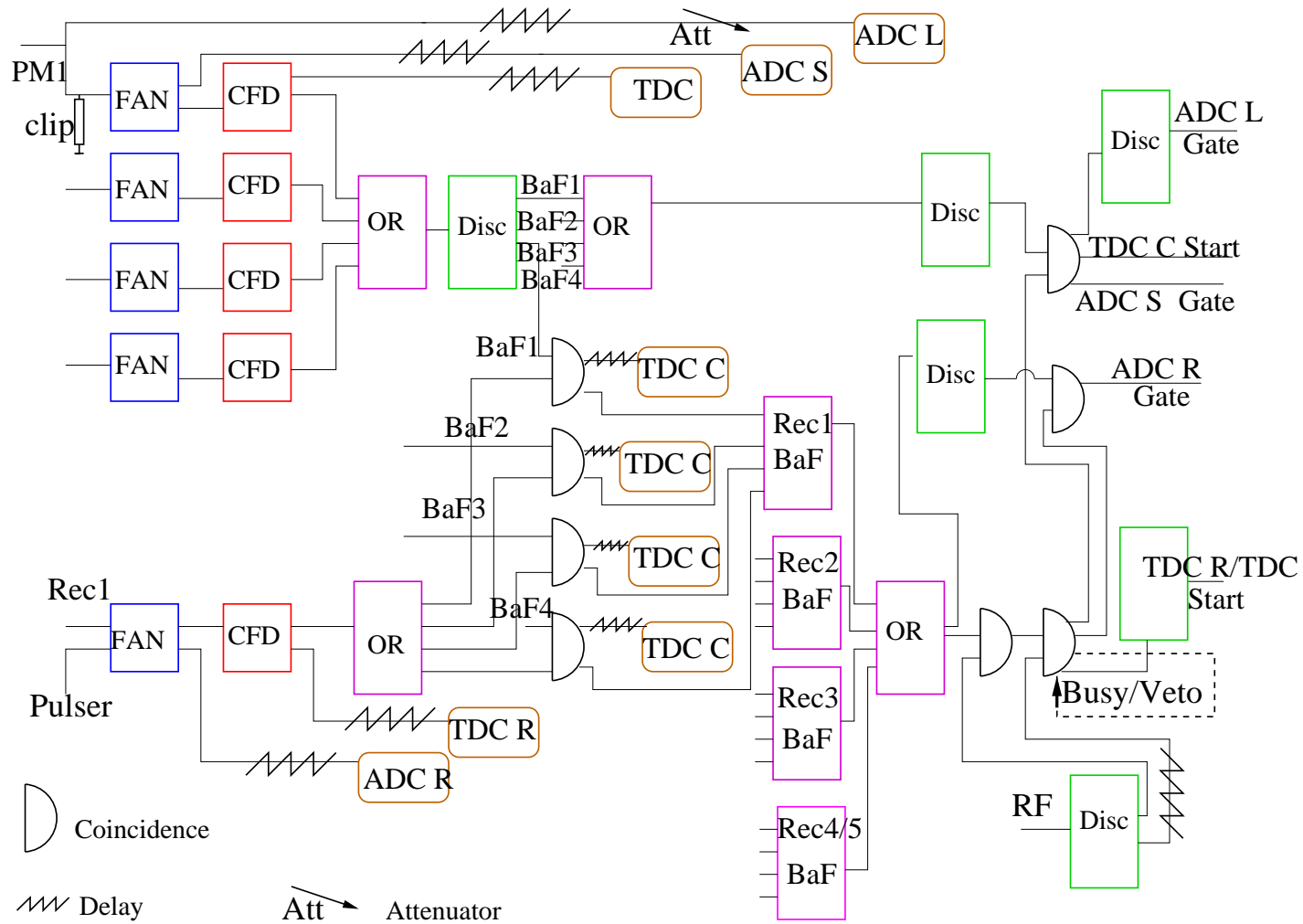
Figure 12: Schematic view of the electronics setup

4 Analysis and background subtraction

Due to the fact that the deuteron spin in this experiment was perpendicular to the scattering plane, the differential cross section of the $\vec{d}p$-capture process can be expressed in terms of analyzing powers A_y, A_{yy} only (see section 2, (11)):

$$d\sigma(\theta) \quad = \quad d\sigma_0(\theta)[1 + \frac{3}{2}P_{\mathcal{Z}}A_y(\theta) + \frac{1}{2}P_{\mathcal{Z}\mathcal{Z}}A_{yy}(\theta)]$$

The cross section for every given polarization state with the polarizations $P_{\mathcal{Z}}^i$, $P_{\mathcal{Z}\mathcal{Z}}^i$ ($i=a$, b, c, d, e) is proportional to the number of capture gammas detected for this polarization state such as

$$N^i K^i = N^0[1 + \frac{3}{2}P_{\mathcal{Z}}^i A_y + \frac{1}{2}P_{\mathcal{Z}\mathcal{Z}}^i A_{yy}], \tag{14}$$

where K^i is the dead time and Faraday cup normalization coefficient to even out the current and dead time difference between different polarization states,

$$K^i = \frac{FC^0}{FC^i} \cdot \frac{1 - DT^0}{1 - DT^i}. \tag{15}$$

Using the information from Table 1 and the equation (14) the following expressions for A_y, A_{yy} were derived:

$$A_{yy}^k \quad = \quad 2 \cdot \frac{\frac{N^i K^i - N^0}{N^0} \cdot P_{\mathcal{Z}}^j - \frac{N^j K^j - N^0}{N^0} \cdot P_{\mathcal{Z}}^i}{P_{\mathcal{Z}\mathcal{Z}}^i \cdot P_{\mathcal{Z}}^j - P_{\mathcal{Z}\mathcal{Z}}^j \cdot P_{\mathcal{Z}}^i}$$

$$A_{yy} \quad = \quad \frac{\frac{1}{(\Delta A_{yy}^1)^2}A_{yy}^1 + \frac{1}{(\Delta A_{yy}^2)^2}A_{yy}^2}{\frac{1}{(\Delta A_{yy}^1)^2} + \frac{1}{(\Delta A_{yy}^2)^2}} \tag{16}$$

where $k=1$, $i = d$, $j = c$ and $k=2$, $i = b$, $j = e$;

$$A_y^k \quad = \quad \frac{2}{3} \cdot \frac{\frac{N^i K^i - N^0}{N^0} \cdot P_{\mathcal{Z}\mathcal{Z}}^j - \frac{N^j K^j - N^0}{N^0} \cdot P_{\mathcal{Z}\mathcal{Z}}^i}{P_{\mathcal{Z}\mathcal{Z}}^i \cdot P_{\mathcal{Z}}^j - P_{\mathcal{Z}\mathcal{Z}}^j \cdot P_{\mathcal{Z}}^i}$$

$$A_y \quad = \quad \frac{\frac{1}{(\Delta A_y^1)^2}A_y^1 + \frac{1}{(\Delta A_y^2)^2}A_y^2}{\frac{1}{(\Delta A_y^1)^2} + \frac{1}{(\Delta A_y^2)^2}} \tag{17}$$

where $k=1$, $i = d$, $j = e$ and $k=2$, $i = b$, $j = c$. The statistical errors ΔA_y^k, ΔA_{yy}^k are given by expressions (23) and (24) in section 4.5, N^i is the integral of the experimental γ-spectrum for the polarization state i.

The gamma spectra were derived from the BaF$_2$ short component by applying the software cuts defined using the time-of-flight and energy information from the recoil- and γ-detectors.

For every BaF$_2$-crystal in a given γ-detector box this information is represented by the following data:

1. time-of-flight spectrum of particles coming to the BaF_2-detector — the distribution of the time difference between "start" RF-signal and "stop" signal of the detector;

2. BaF_2 energy spectrum — the distribution of energy deposited in the BaF_2-detector;

3. time-of-flight spectra of particles coming to the recoil-detectors — the distribution of the time difference between "start" RF-signal and "stop" signals of the detectors;

4. recoil energy spectra — the distribution of energy deposited in the recoil detectors;

5. BaF_2-recoil coincidence time spectra (the coincidences between given γ-detector and given recoil-detector for the online analysis and more detailed information such as the coincidences between given BaF_2-crystal and given recoil-detector for the offline analysis) — the distribution of the time difference between "start" signal from the BaF_2-detector and "stop" signal from the recoil detector.

All these data contain not only the real capture events but also the background events. There are two main sources of background:

- the reaction of deuteron breakup $A(\vec{d}, pn)A$, that gives the coincidences between neutrons and protons as well as the accidental coincidences of gammas and protons and neutrons and ^3He;

- elastic scattering of deuterons from the *havar*-windows of the target cell, that produces the accidental coincidences between deuterons and gammas.

The number of the background events is very significant due to the fact that the cross section of the $\vec{d}p$-capture process is of the order of μb/sr (see Figure 4) and the cross sections of the background reactions are of the order of mb/sr. The software cuts should maximally reject the number of the accidental coincidences between gammas and particles originating from the background reactions. The procedure of applying cuts is described in details in the next subsection using the data at $E_d = 29$ MeV, $\theta_{\gamma\ lab} = 130^0$ as an example. The data for other angles and energy were analyzed using the same method. Cuts were defined and applied independent of the deuteron polarization state.

4.1   Main cuts

The data for all gamma scattering angles were divided into the sets of 20-50 runs. The data within one set were summed up to reduce the statistical

uncertainties of the analysis due to the low capture event rate. To do
this summing correctly, BaF_2 TDC spectra were adjusted to the chosen
reference ones using the gamma-peak channel number as it is shown in
expression (18):

$$TDC_{BaF_2}^{i,corr} = TDC_{BaF_2}^i + N_{\gamma-peak}^{ref} - N_{\gamma-peak}^i, \tag{18}$$

where $N_{\gamma-peak}^i$, $N_{\gamma-peak}^{ref}$ are the gamma-peak channel numbers of a given
and reference spectrum. BaF_2 ADC spectra (only short components) were
corrected using the LED-signals such as

$$\begin{aligned} ADC_{BaF_2}^{i,corr} &= (ADC_{BaF_2}^i - offset_{ADC^i}) \cdot \frac{N_{LED}^{ref} - offset_{ADC^{ref}}}{N_{LED}^i - offset_{ADC^i}} \\ &+ offset_{ADC^{ref}}, \end{aligned} \tag{19}$$

where N_{LED}^i, N_{LED}^{ref} are the LED-signal peak channel numbers and ADC
offsets are defined as the pedestal-peak channel numbers. The raw BaF_2
lightoutput and TOF spectra at $E_d = 29$ MeV, $\theta_{\gamma\ lab} = 130^0$ are presented in
Figure 13. The uncut lightoutput spectrum demonstrates the ratio between
the background and the real capture events. The uncut TOF spectrum re-
presents the gamma-peak and the amount of slower particles (neutrons)
that should be cut off. But there is also a certain amount of background
under the gamma peak. To define the TOF-cuts more accurately, two-
dimensional information about TOF and energy of particles in the BaF_2-
detector was used. This information is presented in Figure 14. The TOF-
region of the most energetic particles (gammas) can be defined and the part
of the energy spectrum which contains mostly low-energy γ and neutron
background can be excluded from the further analysis.

A BaF_2-detector at a given gamma angle has coincidences only with the
recoil detectors fulfilling the ^{3}He-kinematics conditions. The trajectories of
^{3}He were simulated using the code "raytrace" and the corresponding recoil
detectors were determined. In the case of $E_d = 29$ MeV, $\theta_{\gamma\ lab} = 130^0$ the
coincidences were found for the recoil detectors number 2, 3, 4 (number
1 is the closest to the beam line). In Figures 14, 15 a two-dimensional
information about the lightoutput of a given recoil and the correspond-
ing coincidence time (BaF_2 TOF $-$ recoil TOF + positive offset) is pre-
sented. The cuts on BaF_2 TOF and BaF_2-lightoutput are applied. This
two-dimensional information allows us to make the particle identification.
In the second two-dimensional histogram in Figure 14 the slowest parti-
cles are ^{3}He, the fastest ones with the lowest lightoutput are scattered
deuterons; due to their high energy (29 MeV) deuterons loose 1.14 MeV in
the target what leads to a deposited energy of 4.63 MeV. Particles that are
faster than ^{3}He and produce more light in the recoil detector are protons
with a low energy. The relatively large lightoutput in this case results from
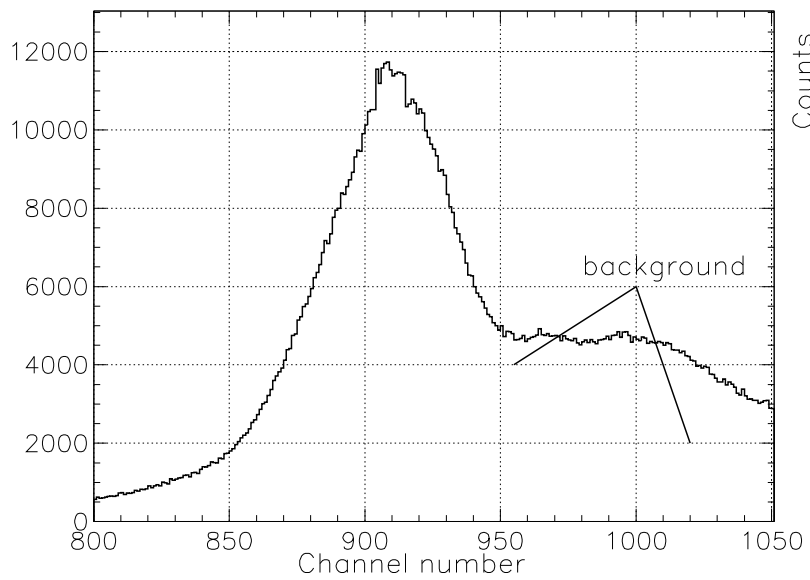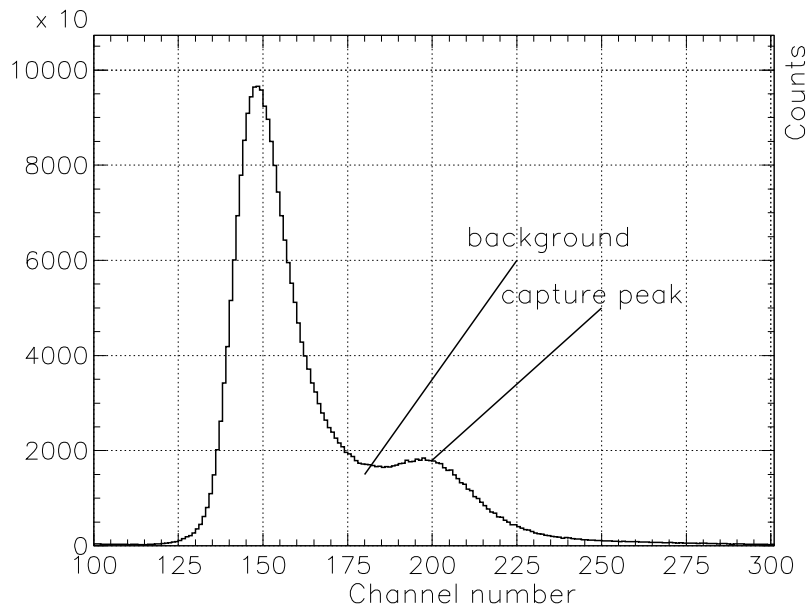
Figure 13: *Raw BaF$_2$ fast component lightoutput and TOF spectra.*
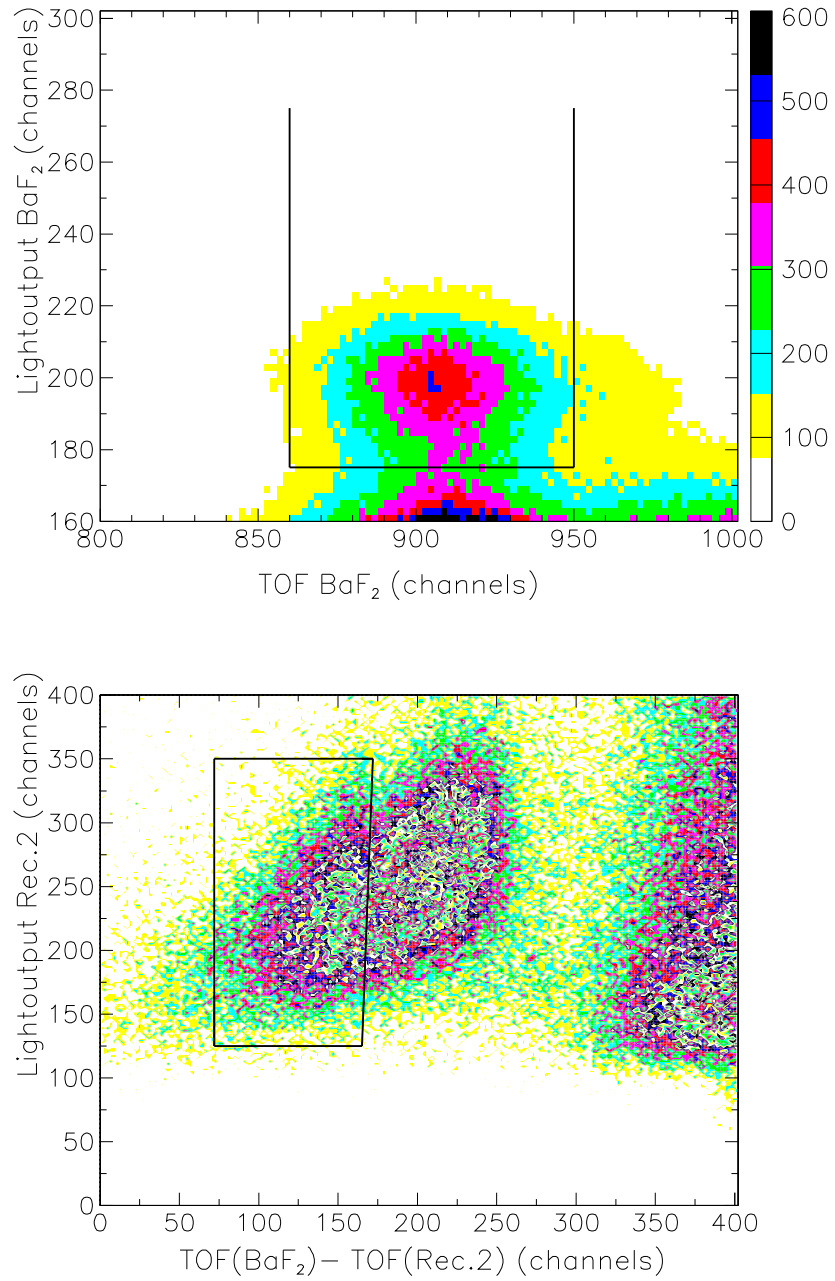
Figure 14: *BaF$_2$ lightoutput VS BaF$_2$ TOF and lightoutput of Rec.2 VS coincidence time. Cuts are shown as the black lines.*
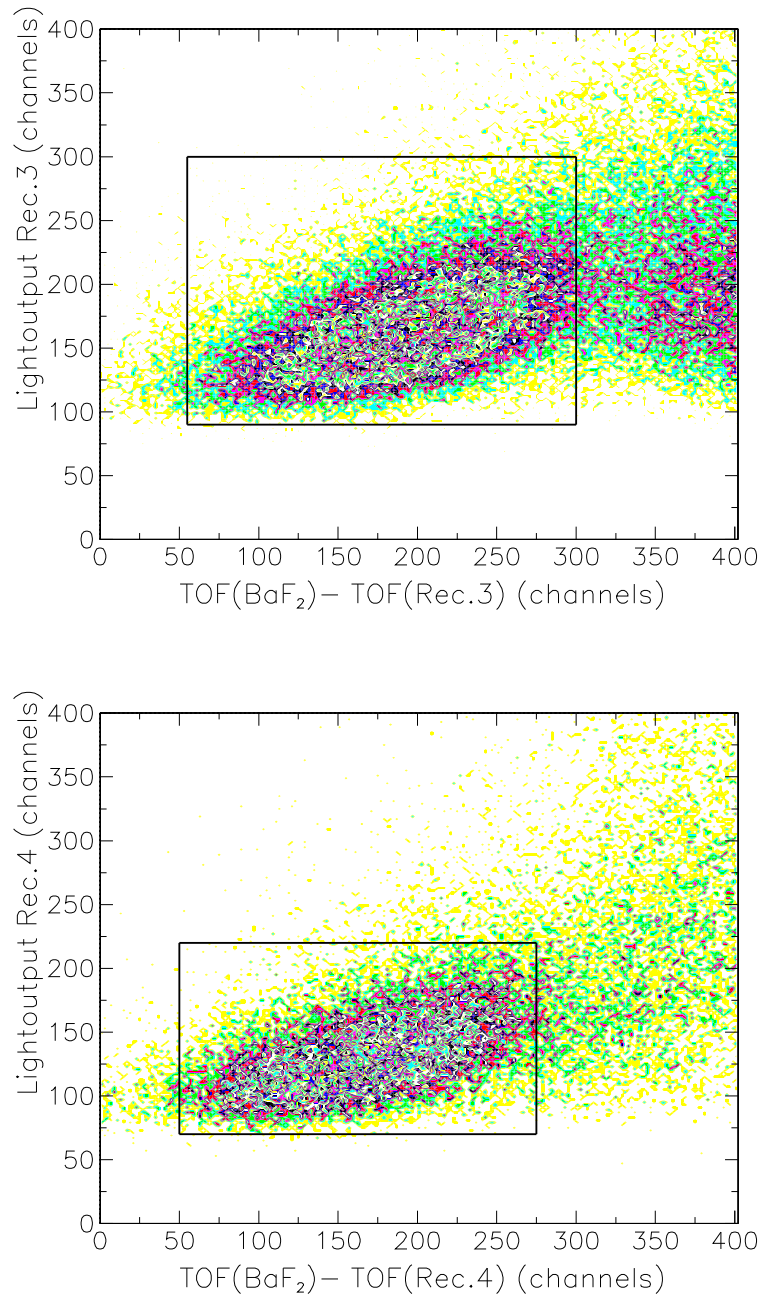
Figure 15: *Lightoutput of Rec.3,4 VS coincidence time. Cuts are shown as the black lines.*
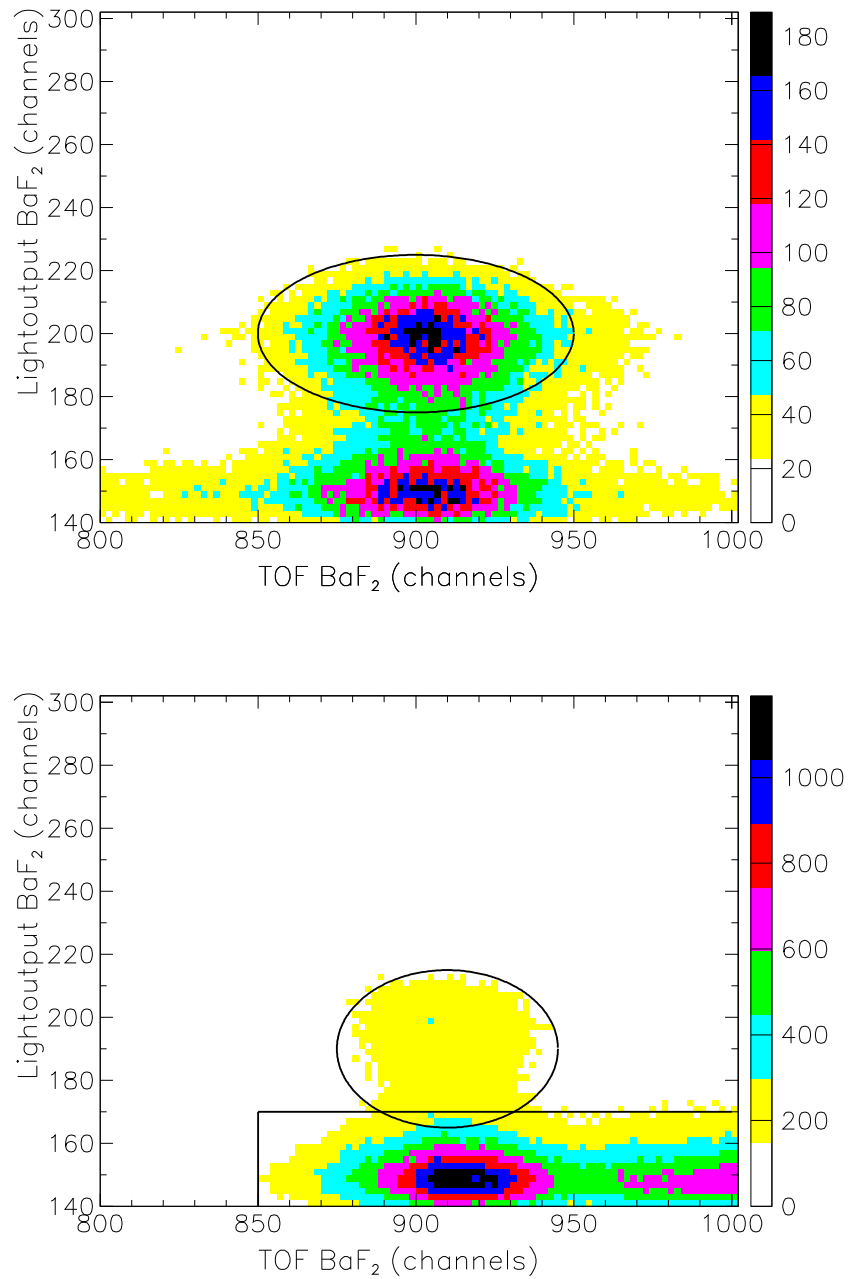
Figure 16: *BaF$_2$ lightoutput VS TOF spectra of particles giving coincidences with ^{3}He (upper plot) or with p and d (lower plot). Different cuts on coincidence time and lightoutput of the recoils are applied.*
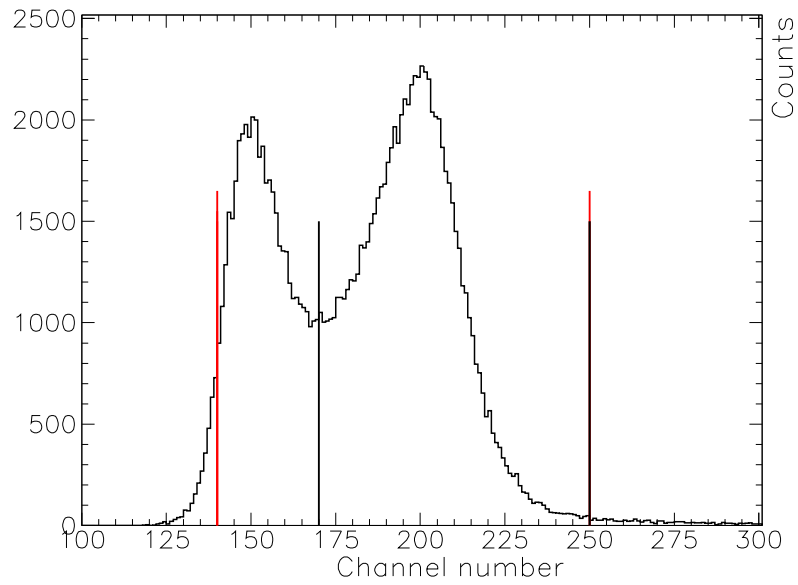
Figure 17: *Experimental γ-spectrum. The black lines show the integration limits used for extraction of A_y, A_{yy} values, the red lines show the integration limits used for test of the background correction.*

the fact that the plastic scintillator lightoutput depends on the incoming particle type (see [27]). It is larger for protons than for ^{3}He. The slowest particles in the first two-dimensional histogram in Figure 15 are also ^{3}He and the faster ones are deuterons. Almost equal lightoutput is caused by the fact that ^{3}He incident on the third recoil detector have lower energy than on the second one due to the difference in energy losses in the target. The second two-dimensional histogram in Figure 15 for the recoil detector number 4 demonstrates that $\gamma-^3$He coincidences can be easily separated from unstructured accidental ones. Thus, the coincidence between gammas and recoil particles can be separated from the $\gamma-p$ and $\gamma-n$ coincidences by applying cuts on coincidence time and lightoutput of the recoil detectors. In Figure 16 two BaF$_2$-lightoutput VS BaF$_2$-TOF spectra of particles giving coincidences with ^{3}He (upper plot) or protons and deuterons (lower plot) are shown. In these two cases different cuts on TDC coincidence and recoil-lightoutput are applied. These spectra provide the quantitative information about the number of ^{3}He$-\gamma$ and $p, d-\gamma$ (within black ellipses) as well as ^{3}He$-n$ and $p, d-n$ (within black rectangle) coincidences.

In Figure 17 a gamma spectrum obtained from the raw BaF$_2$ short component by applying all above described cuts (excepting the cut on BaF$_2$-lightoutput) is presented. The left part of the spectrum is due to low energy neutron and γ background. Some of it contributes to the region of γ-peak within the integration limits what influences on the extracted A_y, A_{yy} values. Thus, to determine the effect of the background contribution and to correct it, the behavior of the background under the capture peak should be known. The background function was extracted from the experimental gamma spectrum using the BaF$_2$ γ-response function. To define the response function, an additional experiment with monoenergetic γ-rays was performed.

4.2 BaF$_2$ gamma response function

The BaF$_2$ gamma response function was determined at the Institute for Physics of the University of Basel using the monoenergetic $\sim$20 MeV γ-rays from the reaction

$$p + T \;\rightarrow\; ^4He + \gamma \quad Q = 19.82 MeV$$
$$\rightarrow\; ^3He + n \quad Q = -0.763 MeV.$$
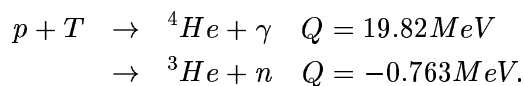
The proton beam with an energy of $\sim$1 MeV (near the neutron threshold) was provided by the Cockroft-Walton accelerator "4MV". The laboratory gamma angle was chosen to be 110° to maximize the gamma-rate (the maximum of the gamma angular distribution is at 90°) and to minimize the amount of neutrons (the maximum of the neutron angular distribution is at $\sim 0^o$ [28]). The distance between the tritium target and the BaF$_2$-detector was 80 cm in order to reproduce the geometry of the $\vec{d}p$-capture

experiment. The schematic view of the experimental setup is presented in Figure 18. The target consisted of a 0.45 mg/cm^2 Ti layer with the ab-
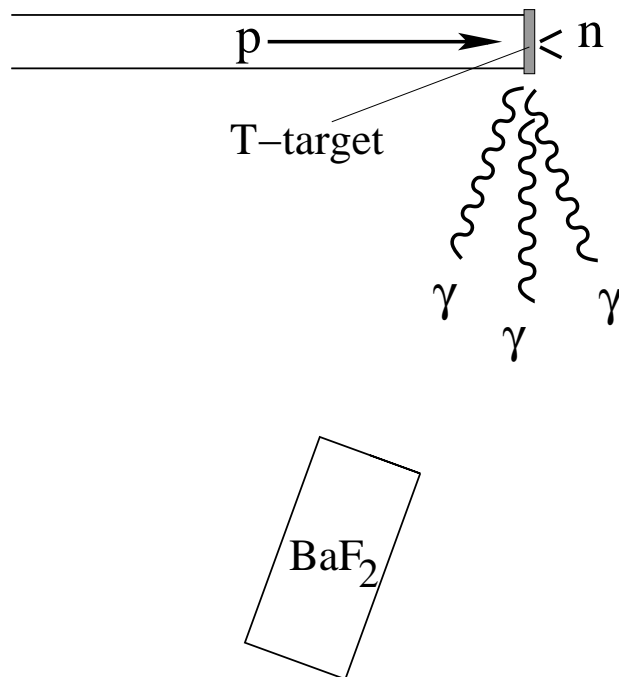
Figure 18: *Schematic view of the experimental setup for the BaF$_2$-detector response function determining.*

sorbed tritium atoms, fixed on a 0.3 mm Cu plate. A simple ice-cooling was enough to prevent the target heating by a $\sim$7 μA continuous proton beam. The electronics was a simplified version of the $\vec{d}p$-capture experiment one without the recoil detectors, coincidences and RF-signal. The same electronic modules and gate widths were used.

In Figures 19 and 20 the short and long component of the BaF$_2$ response function are presented. The cosmic background is subtracted (a long cosmics-run was performed and the amount of cosmic events was adjusted to the run-time).

4.3   Analysis of the γ-spectrum and background correction

The short component of the BaF$_2$ response function was used to define the amount of the low energetic n and γ background under the capture peak (see section 4.1) in the following way: the peak position of the response function was adjusted to the position of the γ-peak in the experimental spectrum and then a sum of an exponential function representing the background and the response function adjusted in height and folded with a Gaussian was fitted to the capture peak region in the experimental spect-

Figure 19: *Short component of the BaF$_2$ response function.*

Figure 20: *Long component of the BaF$_2$ response function.*

rum in order to identify the parameters of the background function (see expression (20)).

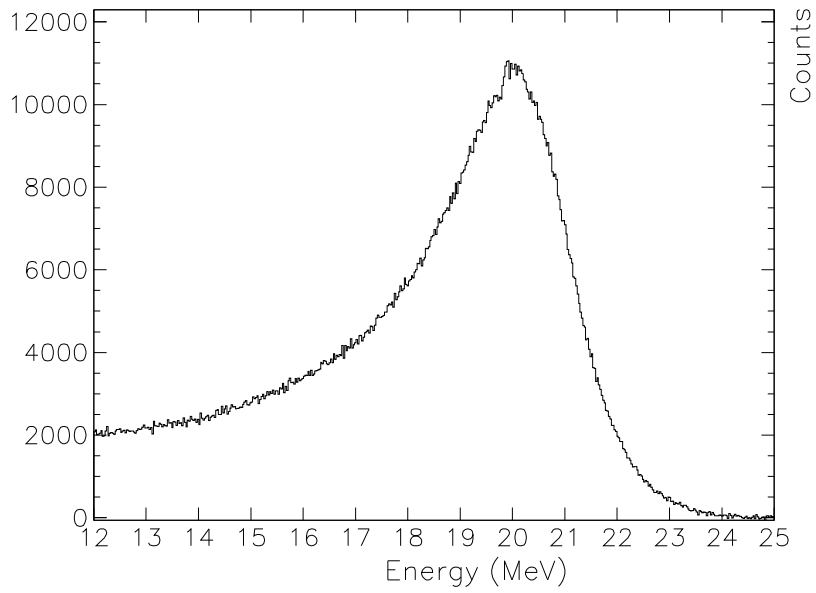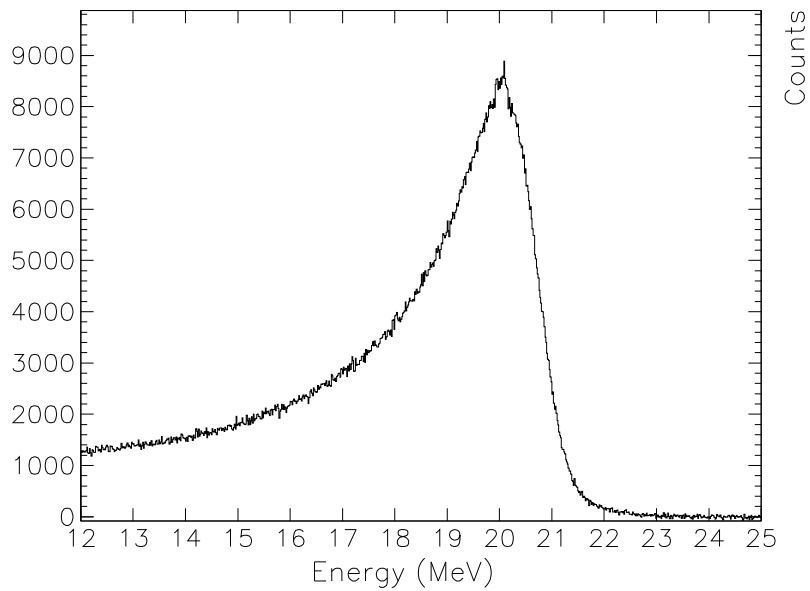$$F(x) = p_1 \cdot e^{-p_2 \cdot x} + \frac{\displaystyle\int_{x-3p_4}^{x+3p_4} p_3 \cdot DRF(\tilde{x}) \cdot e^{-\frac{(\tilde{x}-x)^2}{2 \cdot p_4^2}} \, d\tilde{x}}{\displaystyle\int_{x-3p_4}^{x+3p_4} e^{-\frac{(\tilde{x}-x)^2}{2 \cdot p_4^2}} \, d\tilde{x}} \longrightarrow$$

$$F(i) = p_1 \cdot e^{-p_2 \cdot i} + \frac{\displaystyle\sum_{j=i-3p_4}^{j=i+3p_4} p_3 \cdot DRF(j) \cdot e^{-\frac{(i-j)^2}{2 \cdot p_4^2}}}{\displaystyle\sum_{j=i-3p_4}^{j=i+3p_4} e^{-\frac{(i-j)^2}{2 \cdot p_4^2}}}$$

$$\chi^2 = \sum_{i=1}^{N} \frac{(y(i) - F(i))^2}{y(i) \cdot (N - 4)} \qquad (20)$$

Here p_1, p_2, p_3, p_4 are free fitting parameters to be determined and N is the number of channels involved in the fitting procedure. The reduced χ^2 value varies from 0.8 to 3.2. An example of this kind of analysis is presented in Figure 21.

The integral of the background function was used to calculate the background correction coefficient for the extracted A_y, A_{yy} values. The low-energy background had nearly zero analyzing powers (more details are given in section 4.4). In this case the true $\vec{d}p$-capture analyzing power values are given by the expressions (21).

$$A_y^{capture} = A_y^{extracted} \cdot \frac{N^{tot}}{N^{tot} - N^{backgr}}$$

$$A_{yy}^{capture} = A_{yy}^{extracted} \cdot \frac{N^{tot}}{N^{tot} - N^{backgr}} \qquad (21)$$

Here N^{tot} is the total number of events within the integration limits and N^{back} is the integral of the background function within the integration limits, $A_y^{extracted}$ and $A_{yy}^{extracted}$ are calculated using the expressions (16), (17). The correction coefficient $\frac{N^{tot}}{N^{tot}-N^{backgr}}$ is angle- and energy-dependent. The values of this ratio for different angles and energies are presented in section 6 in Table 3.
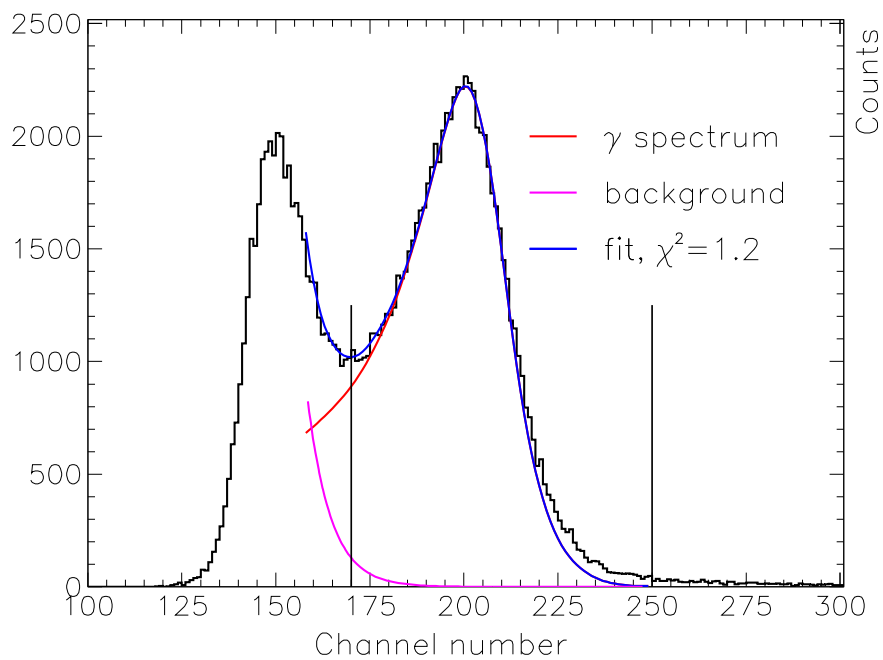
Figure 21: *Experimental γ-spectrum in comparison with the fit-function, reproduced clean γ-spectrum and the background function. The integration limits are represented by two vertical lines.*

4.4   Test of the background correction

The true analyzing powers of the $\vec{d}p$-capture process were calculated under the assumption that the background analyzing powers are zero. This assumption can be tested in the following way.

The amount of the background under the capture peak is very low and if the background is unpolarized, the only systematical effect is the underestimation of the extracted A_y, A_{yy} values by $1 \div 4$ %. This is significantly smaller than the statistical errors of A_y and A_{yy}. It means that different sets of runs at a given θ_γ with different $\frac{N^{tot}}{N^{tot} - N^{backgr}}$ ratios should give the same extracted A_y and A_{yy} values within statistical errors. This was checked for all analyzed angles and no systematic deviations were found. Examples of A_y^k and A_{yy}^k (k=1, 2) as functions of the ratio $\frac{N^{tot} - N^{backgr}}{N^{tot}}$ are presented in Figures 24, 25. Then, if the analyzing powers of the background would not be zero, they would contribute to the extracted analyzing power values according to equations (22).

$$A_{y,\,yy}^{extracted} = A_{y,\,yy}^{capture} \cdot \frac{N^{tot} - N_{back}}{N^{tot}} + A_{y,\,yy}^{back} \cdot \frac{N^{back}}{N^{tot}} \rightarrow$$

$$A_{y,\,yy}^{capture} = A_{y,\,yy}^{extracted} \cdot \frac{N^{tot}}{N^{tot} - N^{backgr}} - A_{y,\,yy}^{back} \cdot \frac{N^{back}}{N^{tot} - N^{backgr}} \quad (22)$$

Thus, if the background contribution is large, it would not be possible to reconstruct the true capture analyzing power values by multiplication of the extracted analyzing powers by the correction coefficient (see expressions (21)). To check it, the experimental γ-spectra at E_d=29 MeV, θ_γ=30° and θ_γ=130° were integrated including low-energy part (the integration limits are shown with the red lines in Figure 17) and the analyzing powers were calculated. Then obtained $A_y^{extracted}$, $A_{yy}^{extracted}$ values were multiplied by the ratio $\frac{N^{tot}}{N^\gamma}$ according to the expressions (21). Here N^γ is the number of capture events within larger integration limits, N^{tot} is the total number of events within larger integration limits. N^γ was obtained by integrating a clean γ-spectrum reproduced by fitting BaF$_2$ response function to the experimental spectrum as it's described in section 4.3. These corrected analyzing powers were compared to the capture analyzing powers. The results of this comparison are presented in Figures 22, 23. The analyzing powers calculated with the larger integration limits are consistent with the analyzing powers calculated for the capture peak for both angles within the statistical errors. These angles were chosen because they represent two extreme cases: minimal background correction in $A_{yy}^{capture}$, $A_y^{capture}$ at θ_γ=130° and maximal one at θ_γ=30°. This check can not be done for E_d=45 MeV because almost all background was cut by the threshold of the electronics, but it has no influence on the results due to the negligibly small amount of the background in the gamma-spectra.

Figure 22: A_y, A_{yy} as functions of the ratio $\frac{N^{tot}}{N^\gamma}$ at $\theta_\gamma=130^o$, $E_d=29$ MeV. The black squares represent the true capture analyzing power values calculated for the capture peak, the red squares represent the analyzing powers calculated for the whole spectra and corrected by the ratio $\frac{N^{tot}}{N^\gamma}$.
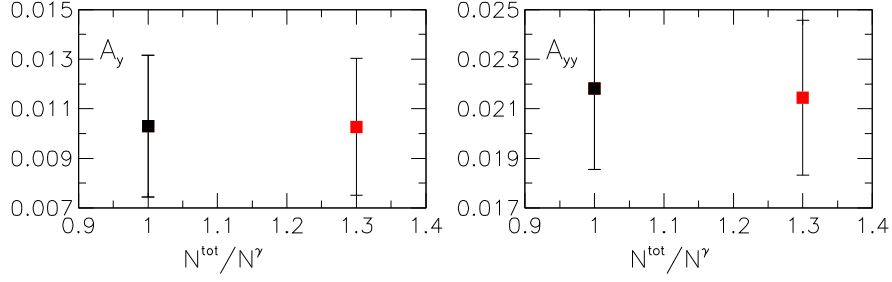

Figure 23: A_y, A_{yy} as functions of the ratio $\frac{N^{tot}}{N^\gamma}$ at $\theta_\gamma=30^o$, $E_d=29$ MeV. The black squares represent the true capture analyzing power values calculated for the capture peak, the red squares represent the analyzing powers calculated for the whole spectra and corrected by the ratio $\frac{N^{tot}}{N^\gamma}$.
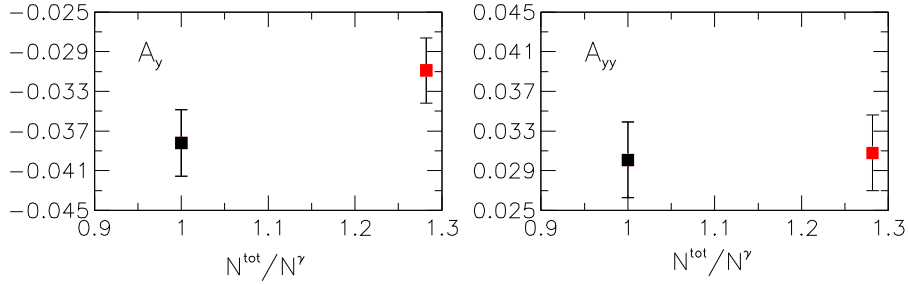
4.5   Error estimation

The statistical errors of A_y and A_{yy} are given by the expressions (23) and (24) which were derived using [22].

$$
\Delta A_y^k = \frac{2 \cdot \sqrt{(\frac{K^i \cdot P_{ZZ}^j}{N^0})^2 \cdot N^i + (\frac{K^j \cdot P_{ZZ}^i}{N^0})^2 \cdot N^j + N^0 \cdot (\frac{N^i K^i \cdot P_{ZZ}^j}{(N^0)^2} - \frac{N^j K^j \cdot P_{ZZ}^i}{(N^0)^2})^2}}{3 \cdot (P_{ZZ}^i \cdot P_Z^j - P_{ZZ}^j \cdot P_Z^i)}
$$
$$
k = 1, \ i = d, \ j = e; \quad k = 2, \ i = b, \ j = c. \tag{23}
$$

$$
\Delta A_{yy}^k = \frac{2 \cdot \sqrt{(\frac{K^i \cdot P_Z^j}{N^0})^2 \cdot N^i + (\frac{K^j \cdot P_Z^i}{N^0})^2 \cdot N^j + N^0 \cdot (\frac{N^i K^i \cdot P_Z^j}{(N^0)^2} - \frac{N^j K^j \cdot P_Z^i}{(N^0)^2})^2}}{(P_{ZZ}^i \cdot P_Z^j - P_{ZZ}^j \cdot P_Z^i)}
$$
$$
k = 1, \ i = d, \ j = c; \quad k = 2, \ i = b, \ j = e. \tag{24}
$$

The total statistical errors are finally given by the equations (25) :

$$
\Delta A_y = \frac{\sqrt{(\Delta A_y^1)^2 + (\Delta A_y^2)^2}}{\frac{\Delta A_y^2}{\Delta A_y^1} + \frac{\Delta A_y^1}{\Delta A_y^2}}
$$

$$
\Delta A_{yy} = \frac{\sqrt{(\Delta A_{yy}^1)^2 + (\Delta A_{yy}^2)^2}}{\frac{\Delta A_{yy}^2}{\Delta A_{yy}^1} + \frac{\Delta A_{yy}^1}{\Delta A_{yy}^2}} \tag{25}
$$

The sources of the systematical effects are the background correction coefficients, the normalization coefficients K^i (see (15)) and the uncertainties in the polarization values.

The systematical error due to the background correction coefficient was calculated under assumption that the uncertainty in the number of background events under the capture peak is not more than 10% of its value.

The normalization coefficients K^i as a source of the systematical effects were investigated first using A_y^k, A_{yy}^k values calculated with different polarization states (see (17) and (16)). A disagreement between A_y^k, A_{yy}^k for k=1 and k=2 would be a sign of such effects, but the analyzing powers are consistent within the statistical errors for all angles and for both deuteron energies. The examples are presented in Figures 22, 23. It means that these systematic effects are smaller than the statistical errors. The numerical value of a freak asymmetry due to the correlation of polarization state and beam current was calculated using the following procedure: two runs with different average current were chosen, then the numbers of events in zero-polarization state were scaled to each other using the dead-time and current normalization coefficient and the freak asymmetry was calculated according to equation (26).

$$
A^{freak} = \frac{N_0' \cdot \frac{FC_0 \cdot (1-DT_0)}{FC_0' \cdot (1-DT_0')} - N_0}{N_0}, \tag{26}
$$

$$A^{freak} = 0.29 \ \ at \ E_d = 29 \ MeV \ \ for \ \ \Delta I = 14.4 \ nA - 11.0 \ nA \equiv 3.4 \ nA,$$
$$A^{freak} = 0.12 \ \ at \ E_d = 45 \ MeV \ \ for \ \ \Delta I = 14.3 \ nA - 12.8 \ nA \equiv 1.5 \ nA.$$

The difference in current between different polarization states was about 0.005 nA at E_d=29 MeV and 0.003 nA at E_d=45 MeV. Thus, the systematical error values can be calculated by scaling the freak asymmetry to the experimental current difference. The following values were obtained:

$$\delta A^{freak} = 0.00043 \ \ at \ E_d = 29 \ MeV,$$
$$\delta A^{freak} = 0.00024 \ \ at \ E_d = 45 \ MeV.$$

The errors coming into the extracted A^k_{yy} values due to the uncertainties in the polarization values were estimated using equations (27):

$$\delta^i_{P_\mathcal{Z}} A^k_{yy} = A^k_{yy}(P^i_\mathcal{Z}) - A^k_{yy}(P^i_\mathcal{Z} + \Delta P^i_\mathcal{Z})$$
$$\delta^i_{P_{\mathcal{Z}\mathcal{Z}}} A^k_{yy} = A^k_{yy}(P^i_{\mathcal{Z}\mathcal{Z}}) - A^k_{yy}(P^i_{\mathcal{Z}\mathcal{Z}} + \Delta P^i_{\mathcal{Z}\mathcal{Z}})$$
$$\delta A^k_{yy} = \sqrt{\sum_i ((\delta^i_{P_\mathcal{Z}} A^k_{yy})^2 + (\delta^i_{P_{\mathcal{Z}\mathcal{Z}}} A^k_{yy})^2)},$$
$$k = 1, \ 2. \tag{27}$$

The total A_{yy} error due to the polarization values uncertainties is finally given by equation (28):

$$\delta A_{yy} = \frac{\sqrt{\frac{(\delta A^1_{yy})^2}{(\Delta A^1_{yy})^4} + \frac{(\delta A^2_{yy})^2}{(\Delta A^2_{yy})^4}}}{\frac{1}{(\Delta A^1_{yy})^2} + \frac{1}{(\Delta A^2_{yy})^2}} \tag{28}$$

The same procedure was applied to A_y.
The total systematic errors were calculated, their values are given in section 6 in Tables 4, 5, 6, 7.
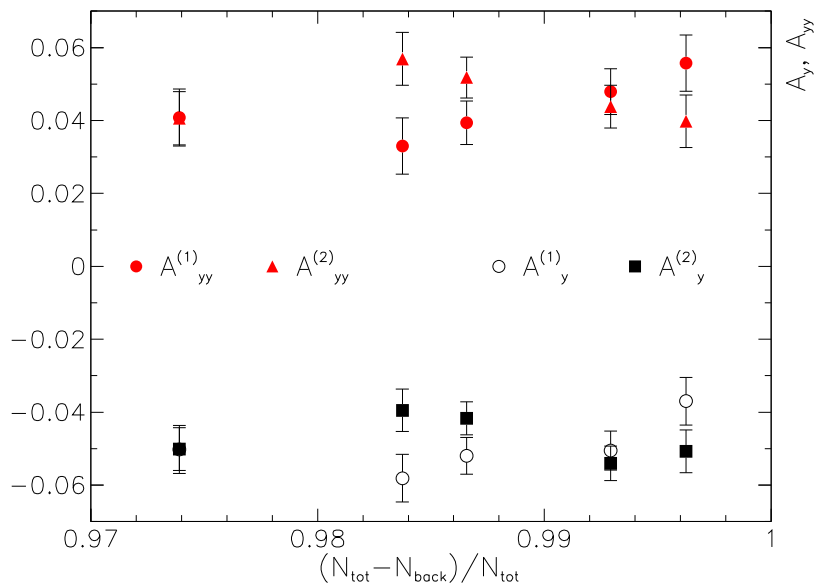
Figure 24: A_y, A_{yy} as functions of the events-to-background ratio at $\theta_\gamma = 27^o$, $E_d = 45$ MeV.
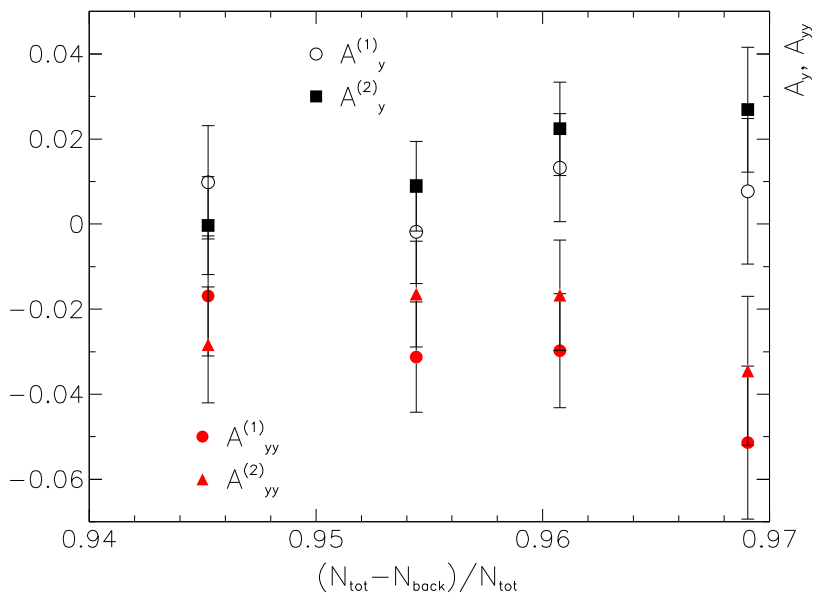

Figure 25: A_y, A_{yy} as functions of the events-to-background ratio at $\theta_\gamma = 169^o$, $E_d = 29$ MeV .

5 Theoretical calculations of A_y, A_{yy}

The calculations of A_y, A_{yy} of the $\vec{d}p$ - capture process for E_d =29 MeV and E_d =45 MeV were performed by the group of J. Golak, K. Kamada, H. Wita\l{}a, W. Glöckle, R. Skibinski et al. They were based on the AV18 potential and the Urbana IX 3NF.

The potential is constructed on the base of the Argonne V14 and Urbana V14 potentials especially to reproduce correctly both np and pp scattering data. It is represented in an operator format as a sum of 18 spin and isospin dependent operators.

$$
\begin{aligned}
v_{ij} &= \sum_{p=c,\sigma,t,ls,l2,l2\sigma,ls2} [v_{ij}^p(r_{ij}) + v_{ij}^{p\tau}(r_{ij})\hat{\tau}_i \cdot \hat{\tau}_j]\hat{O}_{ij}^p \\
&+ v_{ij}^T(r_{ij})T_{ij} + v_{ij}^{\sigma T}(r_{ij})(\hat{\sigma}_i \cdot \hat{\sigma}_j)T_{ij} + v_{ij}^{tT}(r_{ij})S_{ij}T_{ij} \\
&+ v_{ij}^{\tau z}(r_{ij})(\hat{\tau}_{z,i} + \hat{\tau}_{z,j}),
\end{aligned} \tag{29}
$$

where

$$
\hat{O}^{p=c,\sigma,t,ls,l2,l2\sigma,ls2} = 1, \hat{\sigma}_i \cdot \hat{\sigma}_j, \hat{S}_{ij}, (\hat{\mathbf{L}} \cdot \hat{\mathbf{S}})_{ij}, \hat{\mathbf{L}}^2, \hat{\mathbf{L}}^2\hat{\sigma}_i \cdot \hat{\sigma}_j, (\hat{\mathbf{L}} \cdot \hat{\mathbf{S}})^2
$$

$S_{ij} = 3\hat{\sigma}_i \cdot \hat{r}_{ij}\hat{\sigma}_j \cdot \hat{r}_{ij} - \hat{\sigma}_i \cdot \hat{\sigma}_j$, $T_{ij} = 3\hat{\tau}_{z,i}\hat{\tau}_{z,j} - \hat{\tau}_i \cdot \hat{\tau}_j$, $\hat{\mathbf{S}}$ and $\hat{\mathbf{L}}$ are the total spin and orbital angular momentum operators of pair ij. $\hat{\sigma}_i$, $\hat{\tau}_i$ are the spin and isospin operators of the nucleon i. The last four terms in equation (29) are related to charge symmetry breaking of the NN interaction. The strengths of all terms ($\sim$40 free fitting parameters) were determined by fitting the np and pp experimental data (phase shifts). This phenomenological potential converted to the momentum space representation provides the basis for the three-body Hamiltonian given by equation (1).

The 3N-part of this Hamiltonian was described with the Urbana IX model [29]. This model is based on the Fujita-Miyazawa 3NF, which is supplemented by a phenomenological spin-isospin independent short-range repulsive component. The main contribution in the 3N interaction is given by the 2π exchange between three nucleons with one intermediate Δ excitation. The strength of the 2π-term is chosen such, that the 3N Hamiltonian allows to reproduce the observed binding energy of ^{3}H. The strength of the repulsive term is adjusted to obtain the empirical equilibrium density of nuclear matter. The expression for the Urbana IX 3NF can be found in [29], the following strengths are used in the present calculations: $A_{2\pi} = -0.0293$ MeV, U_0=0.0048 MeV.

The Hamiltonian (1) including and excluding the 3NF term was used to treat both bound and scattering states in the $\vec{d}p$-capture process by solving the corresponding Faddeev equations [10], [11], [12].

The current operator was treated using two different approaches: explicit MEC's [9], [10] and the Siegert theorem [14]. The current operator must

satisfy the continuity equation

$$\hat{\mathbf{q}} \cdot \hat{\mathbf{j}}(\mathbf{q}) \;\; = \;\; [\hat{H}, \hat{\rho}(\mathbf{q})], \tag{30}$$

where $\hat{H}, \hat{\mathbf{j}}(\mathbf{q})$ are given by equations (1), (2) cut on the two-body part and $\hat{\rho}(\mathbf{q})$ is given by equation (31).

$$\hat{\rho}(\mathbf{q}) \;\; = \;\; \sum_i \hat{\rho}_i^{(1)}(\mathbf{q}) + \sum_{i<j} \hat{\rho}_{ij}^{(2)}(\mathbf{q}) + \ldots \tag{31}$$

The continuity equation (30) can be split into the continuity equations for one- and two-body current operators. The present calculations are restricted to one- and two-body currents. The two-body term includes $NN \leftrightarrow NN$ currents only (there are also $NN \leftrightarrow N\Delta$ and $NN \leftrightarrow \Delta\Delta$ ones). These $NN \leftrightarrow NN$ currents are separated into the model-independent (MI) currents, completely determined by the NN interaction, and model dependent (MD) ones, that are purely transverse and not determined by the continuity equation. Their contributions for momentum transfers less than 1 GeV/c are small and only MI currents are included into the present calculations. The MI two-body current operators are defined by the AV18-potential charge-independent terms which do not commute with the one-body charge operator in the two-body continuity equation (32) [1]:

$$\hat{\mathbf{q}} \cdot \hat{\mathbf{j}}_{ij}^{(2)}(\mathbf{q}) \;\; = \;\; [v_{ij}, e^{i\mathbf{q}\cdot\mathbf{r}_i}\frac{1 + \tau_{z,i}}{2} + i \rightarrow j] \tag{32}$$

It is difficult to fulfill exactly the continuity equation with modern nuclear potentials (AV18 in the present calculations) because due to phenomenological short range terms in these potentials it is not possible to define unambiguously which part of the potential corresponds to a given type of MEC. The continuity equation can be fulfilled only approximately. Only the most important MEC's associated with the central isospin dependent $v_{ij}^{c\tau}$, spin-spin isospin dependent $v_{ij}^{\sigma\tau}$ and tensor isospin dependent $v_{ij}^{t\tau}$ terms are included in the present theoretical calculations using the Riska's prescription [13]. According to Riska, the isospin dependent tensor and spin-spin interaction terms are due to exchange of isospin-1 objects that are associated with vector (V) and pseudo-scalar (PS) amplitudes. The first ones are dominantly due to the ρ-meson exchanges and the second ones are due to the π-meson exchanges. Thus the Riska's method is to determine the generalized pseudo-scalar and vector meson exchange current operators using the known form of the single π-meson and ρ-meson exchange current operators. The momentum-space expressions for these operators can be found in [10], they are defined by the potential factors $v_{\rho S}(k)$, $v_\pi(k)$ and $v_\rho(k)$ satisfying the continuity equation for the single π-and ρ-meson exchange interaction. To obtain the two-body current operators that satisfy the continuity equation for the AV18 potential, one should change the potentials

$v_{\rho S}$, v_π and v_ρ to v_{VS}, v_{PS} and v_V correspondingly and define them in terms of $v^{c\tau}$, $v^{\sigma\tau}$ and $v^{t\tau}$ using the two-body continuity equation.

v_{VS}, v_{PS} and v_V are potential-dependent, so the correctness of the calculations done using explicit MEC's depends on the chosen potential properties. One should also take into account, that possible disagreement of data to the calculations done using explicit MEC's can be caused by the inconsistency of MEC's. There might be also other factors such as using of nonrelativistic currents (and wave-functions).

Another approach to treat two-body currents is the Siegert approach, based on the Siegert theorem [14]. It allows us to convert the partial wave decomposition of the nuclear matrix element of the ^{3}He-photodisintegration process (the opposite to the $\vec{d}p$-radiative capture one) to the multipole expansion [10]:

$$
\begin{aligned}
\mathrm{J}^\lambda(\mathbf{q}) &= \langle \Psi^{(-)}_{\mathbf{p}'f} | \hat{\mathbf{e}}_\lambda(\mathbf{q}) \cdot \hat{\mathbf{j}}(0) | \Psi_{\mathbf{p}^3 He} \rangle = \hat{\mathbf{e}}_\lambda(\mathbf{q}) \cdot \langle \Psi^{(-)}_{\mathbf{p}'f} | \hat{\mathbf{j}}(0) | \Psi_{\mathbf{p}^3 He} \rangle = \\
&- \sqrt{2\pi} \sum_{J\lambda} \lambda^\sigma \sqrt{2J+1} \mathcal{T}^\sigma_{J\lambda}(q) \Rightarrow \mathcal{T}^{el} + \mathcal{T}^{mag},
\end{aligned}
\tag{33}
$$

Then one can split the $\mathcal{T}^{el}$ - term using special algebraic identity into two other terms, one of them contains the expression

$$
\hat{\mathbf{q}} \cdot \langle \Psi^{(-)}_{\mathbf{p}'f} | \hat{\mathbf{j}}(0) | \Psi_{\mathbf{p}^3 He} \rangle.
$$

It can be converted using the continuity equation (30) into the term :

$$
\begin{aligned}
\hat{\mathbf{q}} \cdot \langle \Psi^{(-)}_{\mathbf{p}'f} | \hat{\mathbf{j}}(0) | \Psi_{\mathbf{p}^3 He} \rangle &= \langle \Psi^{(-)}_{\mathbf{p}'f} | [\hat{H}, \hat{\rho}(0)] | \Psi_{\mathbf{p}^3 He} \rangle = \\
\langle \Psi^{(-)}_{\mathbf{p}'f} | (E'\hat{\rho}(0) - E\hat{\rho}(0)) | \Psi_{\mathbf{p}^3 He} \rangle &= \omega \langle \Psi^{(-)}_{\mathbf{p}'f} | (\hat{\rho}(0) | \Psi_{\mathbf{p}^3 He} \rangle,
\end{aligned}
\tag{34}
$$

where $\omega = |\mathbf{q}| = q$ is the photon energy. The last term in (34) is the charge density matrix element. It allows us to shift the two-body effects from the current matrix element into the better known charge density matrix element. The other part of the electric term and the magnetic part of (33) are presented in the recent theoretical calculations in the single nucleon current approximation. The procedure described above was done in momentum space, the calculations were not restricted to the long-wavelength approximation and low multipoles only.

The applicability of the Siegert approach is restricted by the fact, that the two-body effects are included only in some of the electric multipoles, the remaining ones are calculated in the single nucleon current approximation. The $\vec{d}p$-capture polarization observables are expected to be correctly described by this type of calculations in the region of medium angles, where E1 dominates, but not at the forward and backward angles, where the magnetic transitions contribute significantly (see [31], [30]).

6   Results and discussion

The analyzing powers A_y, A_{yy} of the $\vec{d}p$-radiative capture process were measured at various gamma-scattering angles at deuteron energies of 29 MeV and 45 MeV. The A_y, A_{yy} values were calculated using the equations (16) and (17). The background under the capture peak in the γ-spectra was determined using the BaF_2 response function. The calculated background correction coefficients are given in Table 3.   The statistical errors of A_y,

θ_{cm}	E_d (MeV)	$\frac{N^{tot}}{N^{tot}-N^{backgr}}$
31.04^o	45	1.015
51.20^o	45	1.007
112.88^o	45	1.000
137.89^o	45	1.000
170.48^o	45	1.000
33.52^o	29	1.044
55.32^o	29	1.030
76.41^o	29	1.013
116.16^o	29	1.021
134.94^o	29	1.008
153.19^o	29	1.014
170.21^o	29	1.046

Table 3: *Values of the ratio $\frac{N^{tot}}{N^{tot}-N^{backgr}}$ for different θ_{cm} at E_d=45 MeV and E_d=29 MeV.*

A_{yy} were calculated using the expressions (23), (24), (25).   The possible sources of the systematical effects were investigated in section 4.5 and the values of the systematical errors were calculated using equations (27), (28). The A_y, A_{yy} values together with their statistical and systematical errors are shown in Tables 4, 5, 6, 7.

The experimental results were compared to the theoretical calculations performed by the group of J. Golak, K. Kamada, H. Witała, W. Glöckle, R. Skibinski et al. The details about the theoretical calculations are given in section 5. To do this comparison correctly, the experimental acceptances were taken into account using the following procedure: the theoretically calculated $A_y(\theta_{cm})$, $A_{yy}(\theta_{cm})$ were folded with the corresponding differential cross section $\sigma(\theta_{cm})$ (see Figure 4) within the angular acceptance of

the γ-detector at a given angle as it is shown in expression (35).

$$A_{yy}^{tot}(\theta_{cm}) = \frac{\sum\limits_{\theta_{cm\ min}}^{\theta_{cm\ max}} A_{yy}(\tilde{\theta}_{cm}) \cdot \sigma(\tilde{\theta}_{cm})}{\sum\limits_{\theta_{cm\ min}}^{\theta_{cm\ max}} \sigma(\tilde{\theta}_{cm})}$$

$$A_{y}^{tot}(\theta_{cm}) = \frac{\sum\limits_{\theta_{cm\ min}}^{\theta_{cm\ max}} A_{y}(\tilde{\theta}_{cm}) \cdot \sigma(\tilde{\theta}_{cm})}{\sum\limits_{\theta_{cm\ min}}^{\theta_{cm\ max}} \sigma(\tilde{\theta}_{cm})} \tag{35}$$

The determined $A_{y}^{tot}(\theta_{cm})$, $A_{yy}^{tot}(\theta_{cm})$ values for given θ_{cm} were connected by a spline-fit for eye-guiding. The results of this comparison are presented in Figures 26 and 27.
The experimental A_{yy} values for E_d=45 MeV are presented in Figure 26. A_{yy} at the middle angle θ_{cm}=113° demonstrates a very good agreement (deviation is less than 1.5σ) with the calculations done using the Siegert approach including 3NF. The A_{yy} value for the very forward angle θ_{cm}=31° is far from all types of calculations. A_{yy} at θ_{cm}=51.2^o differs from the calculations done with the Siegert approach excluding 3NF by 3.5σ. The behavior of A_{yy} at the backward angles is completely different from that predicted by all theoretical calculations. It is confirmed by the fact that the values from the recent experiment agree with the data from the experiment by H. Anklin in this region of angles. The behavior of A_y at E_d=45 MeV is described by the calculations done using explicit MEC's only qualitatively. The Siegert approach gives even worse results.
Figure 27 demonstrates that the experimental values of A_{yy} at E_d= 29 MeV at all measured angles except θ_{cm}=170.2^o are in a perfect agreement with the calculations done with the explicit MEC's approach including 3NF − the deviations are less than 1σ for all angles. A_{yy} at θ_{cm}=170.2^o is far from all types of calculations. The A_{yy} value at θ_{cm}=96.7^o measured in 1985 [30] does not contradict to the data from the present experiment, but this point is a bit out of range. The experimental A_y values demonstrate very good agreement with the calculations done using explicit MEC's at two backward angles only. A_y at θ_{cm}=153.2^o is also in agreement with the calculations using explicit MEC's including 3NF − the 3NF effects are less than the statistical error. The values at the forward and medium angles are far from all theoretical calculations (the deviation is more than 3σ in all cases).

Table 4: A_{yy} *as a function of* θ_{cm} *together with its statistical and system-atical errors at* E_d=45 MeV.

θ_{cm} (deg)	A_{yy}	Statistical err. $\Delta\ A_{yy}$	Systematical err. $\delta\ A_{yy}$
31.04	$4.610 \cdot 10^{-2}$	$0.228 \cdot 10^{-2}$	$0.113 \cdot 10^{-2}$
51.20	$1.199 \cdot 10^{-2}$	$0.197 \cdot 10^{-2}$	$0.048 \cdot 10^{-2}$
112.88	$1.891 \cdot 10^{-2}$	$0.236 \cdot 10^{-2}$	$0.049 \cdot 10^{-2}$
137.89	$2.014 \cdot 10^{-2}$	$0.171 \cdot 10^{-2}$	$0.068 \cdot 10^{-2}$
170.48	$1.334 \cdot 10^{-2}$	$0.407 \cdot 10^{-2}$	$0.095 \cdot 10^{-2}$

Table 5: A_y *as a function of* θ_{cm} *together with its statistical and systematical errors at* E_d=45 MeV.

θ_{cm} (deg)	A_y	Statistical err. $\Delta\ A_y$	Systematical err. $\delta\ A_y$
31.04	$-5.134 \cdot 10^{-2}$	$0.186 \cdot 10^{-2}$	$0.095 \cdot 10^{-2}$
51.20	$-1.955 \cdot 10^{-2}$	$0.160 \cdot 10^{-2}$	$0.042 \cdot 10^{-2}$
112.88	$1.837 \cdot 10^{-2}$	$0.190 \cdot 10^{-2}$	$0.042 \cdot 10^{-2}$
137.89	$2.986 \cdot 10^{-2}$	$0.139 \cdot 10^{-2}$	$0.057 \cdot 10^{-2}$
170.48	$4.507 \cdot 10^{-2}$	$0.328 \cdot 10^{-2}$	$0.081 \cdot 10^{-2}$

Table 6: A_{yy} as a function of θ_{cm} together with its statistical and systematical errors at E_d=29 MeV.

θ_{cm} (deg)	A_{yy}	Statistical err. $\Delta\ A_{yy}$	Systematical err. $\delta\ A_{yy}$
33.52	$3.010 \cdot 10^{-2}$	$0.383 \cdot 10^{-2}$	$0.090 \cdot 10^{-2}$
55.32	$2.197 \cdot 10^{-2}$	$0.288 \cdot 10^{-2}$	$0.070 \cdot 10^{-2}$
76.41	$2.236 \cdot 10^{-2}$	$0.300 \cdot 10^{-2}$	$0.053 \cdot 10^{-2}$
116.16	$2.452 \cdot 10^{-2}$	$0.289 \cdot 10^{-2}$	$0.054 \cdot 10^{-2}$
134.94	$2.182 \cdot 10^{-2}$	$0.326 \cdot 10^{-2}$	$0.055 \cdot 10^{-2}$
153.19	$0.438 \cdot 10^{-2}$	$0.538 \cdot 10^{-2}$	$0.045 \cdot 10^{-2}$
170.21	$-\ 2.934 \cdot 10^{-2}$	$0.520 \cdot 10^{-2}$	$0.067 \cdot 10^{-2}$

Table 7: A_y as a function of θ_{cm} together with its statistical and systematical errors at E_d=29 MeV.

θ_{cm} (deg)	A_y	Statistical err. $\Delta\ A_y$	Systematical err. $\delta\ A_y$
33.52	$-3.821 \cdot 10^{-2}$	$0.335 \cdot 10^{-2}$	$0.084 \cdot 10^{-2}$
55.32	$-1.808 \cdot 10^{-2}$	$0.252 \cdot 10^{-2}$	$0.061 \cdot 10^{-2}$
76.41	$-0.443 \cdot 10^{-2}$	$0.262 \cdot 10^{-2}$	$0.050 \cdot 10^{-2}$
116.16	$0.465 \cdot 10^{-2}$	$0.253 \cdot 10^{-2}$	$0.051 \cdot 10^{-2}$
134.94	$1.030 \cdot 10^{-2}$	$0.285 \cdot 10^{-2}$	$0.052 \cdot 10^{-2}$
153.19	$0.325 \cdot 10^{-2}$	$0.470 \cdot 10^{-2}$	$0.044 \cdot 10^{-2}$
170.21	$1.097 \cdot 10^{-2}$	$0.412 \cdot 10^{-2}$	$0.060 \cdot 10^{-2}$

Figure 26: A_{yy} (upper plot) and A_y (lower plot) as functions of θ_{cm} for E_d=45 MeV in comparison with the theoretical calculations done using explicit MEC's or the Siegert theorem including and excluding Urbana IX 3NF. The additional experimental A_{yy} values are from [31]. Only statistical errors are shown.
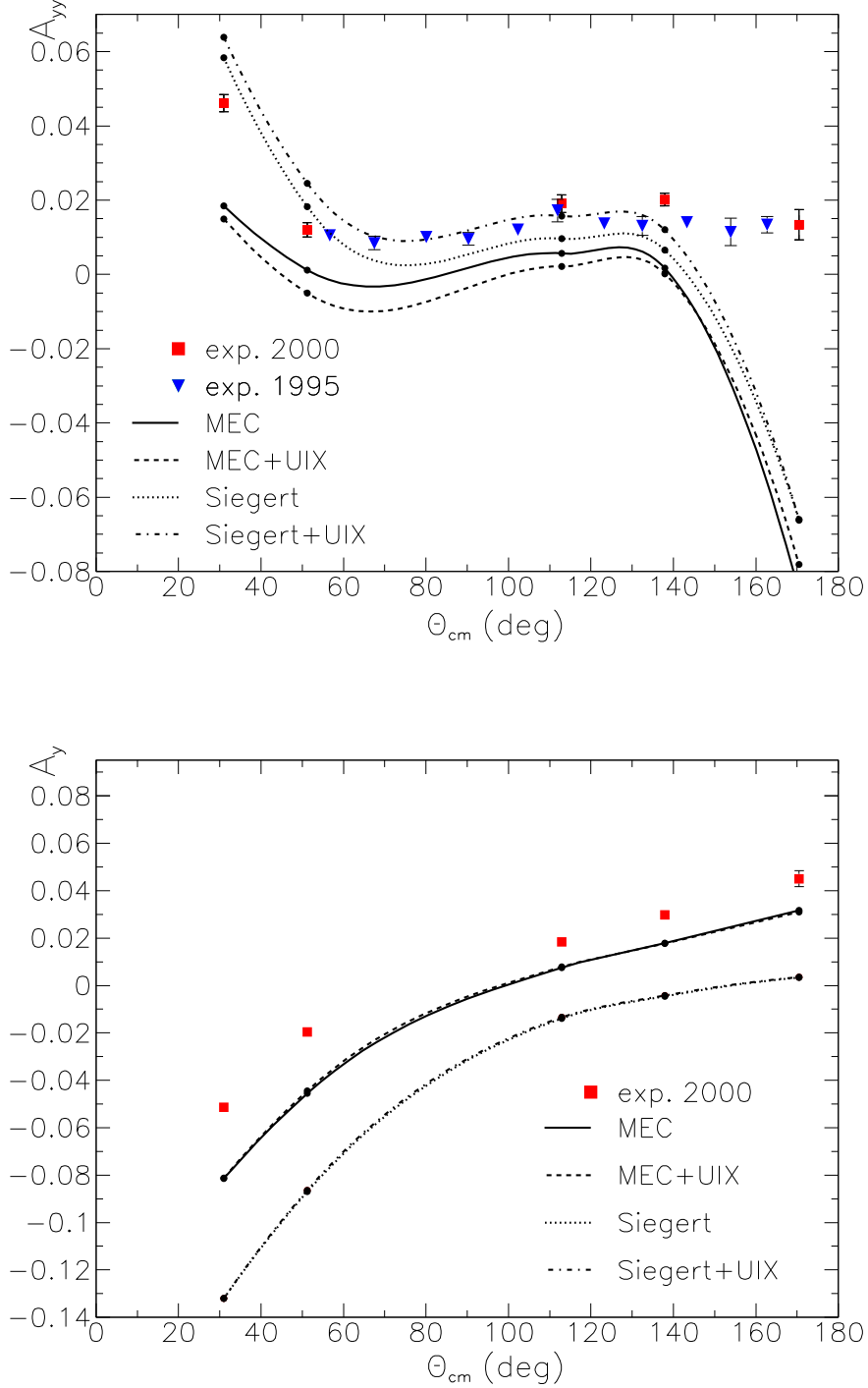
Figure 27: A_{yy} (upper plot) and A_y (lower plot) as functions of θ_{cm} for $E_d=29\,MeV$ in comparison with the theoretical calculations done using explicit MEC's or the Siegert theorem including and excluding Urbana IX 3NF. An additional experimental A_{yy} value is from [30]. Only statistical errors are shown.
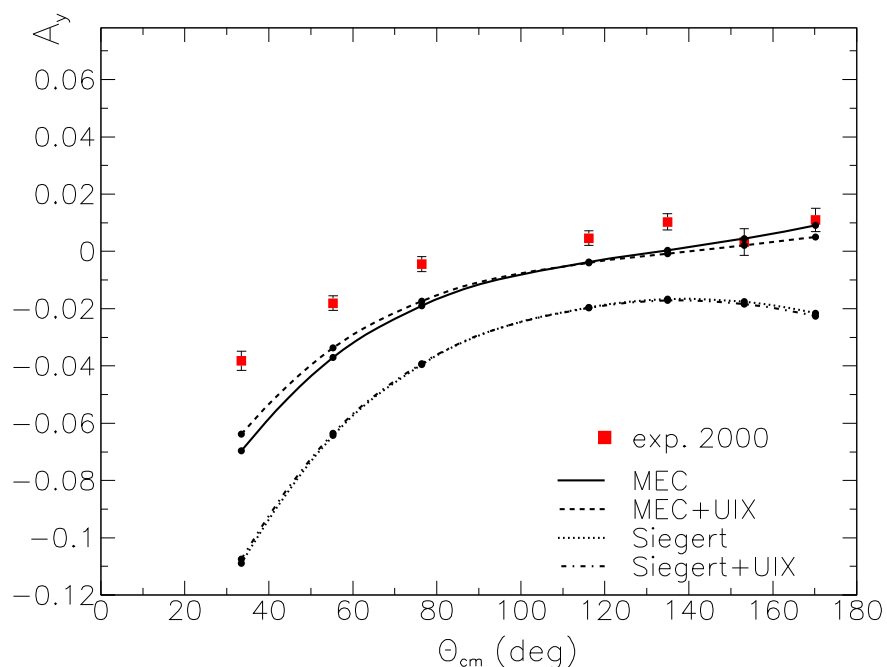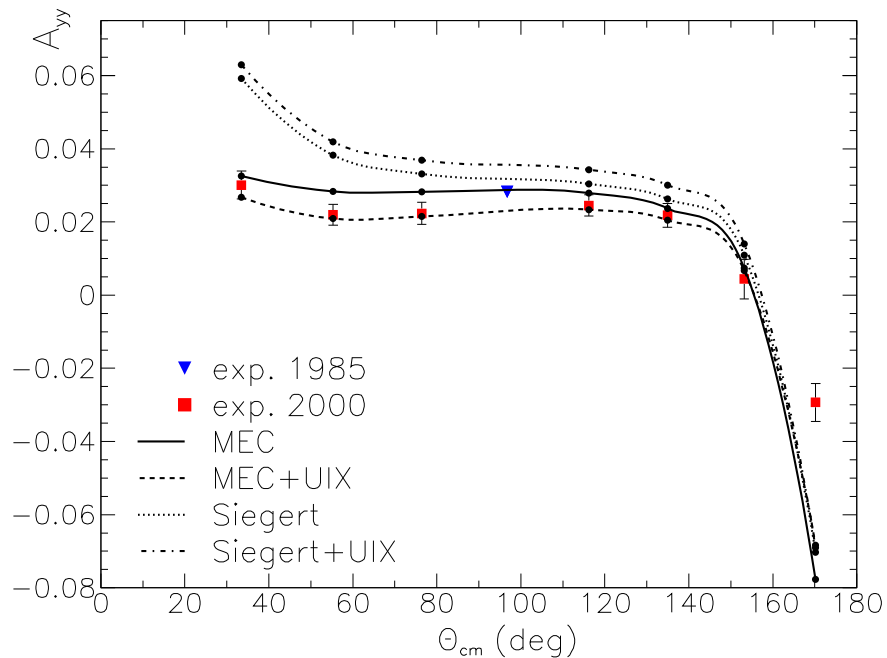
7 Conclusions

The aim of this work was to extend the existing measurements of the analyzing powers A_y, A_{yy} of the $\vec{d} + \text{H} \to \text{He}^3 + \gamma$ reaction. The experimental data were compared to the theoretical calculations done using the Siegert or explicit MEC's approach to treat the electroweak current operator. Three nucleon interaction were included in the calculations in the form of Urbana IX 3NF. The comparison of the calculations to the experimental data provides information about the applicability of the Urbana IX model for description of 3NF effects in the 3N system. It also gives the possibility to test if the MEC effects in the polarization observables can be described with the main NN↔NN model independent meson exchange currents. The results of this comparison are presented in section 6. On the base of these results the following conclusions can be formulated.

The discrepancy between the experimental data and the theoretical calculations done by treating the nuclear current operator with the Siegert approach is due to the fact that the two-body current effects are included only in the electric multipoles which are calculated by changing the current matrix element to the better known charge density matrix element. The rest of the electric multipoles and the magnetic ones are calculated in the single nucleon current approximation. Thus, no adequate description can be obtained for the polarization observables sensitive to the magnetic multipoles. A good example is the behavior of A_{yy} at $E_d=45$ MeV: in the region of medium angles, where A_{yy} is less sensitive to the magnetic multipole contributions (see [31]), A_{yy} can be well described by calculations of this type, but at the forward and backward angles magnetic contributions become important and the Siegert approach fails.

The experimental A_{yy}-data for $E_d=29$ MeV are described by the calculations done using explicit MEC's much better than for $E_d=45$ MeV. To explain this fact, the behavior of A_{yy} as a function of a deuteron energy should be taken into account. The experimental data as well as the theoretical calculations show that A_{yy} at the medium angles (plateau-region) changes slightly from $\sim$10 MeV to $\sim$30 MeV, falls down to cross zero at $\sim$50 MeV and stays negative. The behavior of A_{yy} at $\theta_{\gamma\ lab}=90^o$ as a function of the deuteron energy is given in [33]. The absolute values of the theoretically calculated A_{yy} in the plateau-region at $E_d=45$ MeV are expected to be $\sim$3 times less than at $E_d=29$ MeV. It makes them more sensitive to the uncertainties in treatment of MEC's (MEC's are not fully consistent, no Δ-currents) and to the simplified spin structure of 3NF. In the present calculations nonrelativistic currents and wave-functions were used. A significant disagreement between the theoretical calculations and experimental data at $E_d=45$ MeV might be a sign that the relativistic corrections at higher energy are important.

The theoretical description of A_y for both energies leaves space for improve-

ment. The difference between the experimental data and the theoretical calculations done using explicit MEC's is caused by the above mentioned uncertainties in the treatment of MEC's and the simplified semi-empirical way to describe 3NF. It leads us to the conclusion that more complete treatment of MEC's and a more sophisticated model of 3N interaction are needed to obtain a quantitative agreement between the experimentally measured polarization observables and the theoretical predictions. However, extensions are very difficult due to the fact that modern NN potentials are phenomenological and it is not possible to define unambiguously which part of the potential corresponds to a given type of MEC. Another theoretical approach to construct the NN and 3N forces, based on the use of chiral Lagrangian, might solve this problem [32], [34].

References

[1] R.B. Wiringa et al., *Phys. Rev. C* **51**, 38 (1995).

[2] V.G.J. Stoks et al., *Phys. Rev. C* **49**, 2950 (1994).

[3] R. Machleidt et al., *Phys. Rev. C* **53**, 1483 (1996).

[4] H. Witała et al., *Phys. Rev. Lett.* **81**, 1183 (1998).

[5] Y. Koike and S. Ishikawa, *Nucl. Phys. A* **631**, 683c (1998).

[6] B. S. Pudliner et al., *Phys. Rev. C* **56**, 1720 (1997).

[7] B. S. Pudliner et al., *Phys. Rev. Letters* **74**, 4396 (1995).

[8] K. Sagara et al., *Phys. Rev. C* **50**, 576 (1994).

[9] J. Carlson and R. Schiavilla, *Rev. Mod. Phys.* **70**, 743 (1998).

[10] J. Golak et al., *Phys. Rev. C* **62**, 054005 (2000).

[11] A. Nogga et al., *Phys.Lett. B* **409**, 19 (1997).

[12] J. Golak et al., *Phys. Rev. C* **51**, 1638 (1995).

[13] D.O. Riska, *Phys. Scr.* **31**, 107 (1985); **31**, 471 (1985).

[14] A.J.F. Siegert, *Phys. Rev.* **52**, 787 (1937).

[15] M. Viviani et al., *Phys. Rev. C* **54**, 534 (1996).

[16] *Proc. Third Int. Symp. on polarization phenomena in nuclear reactions*, ed. H. H. Barschall and W. Haeberli (Uniteraity of Wisconsin Press, 1971, p.xxv).

[17] G.G. Ohlsen et al., *Nucl. Instr. and Methods* **179**, 283 (1981).

[18] G.G. Ohlsen , *Rep. Prog. Phys.* **35**, 717 (1972).

[19] W. Haeberli , *Ann. Rev. Nucl. Sci.* **17**, 373 (1967).

[20] H. Anklin, *PhD Thesis*, University of Basel, 1998.

[21] D. Singy et al., *Nucl. Instr. and Methods B* **47**, 167 (1990).

[22] P.R. Bevington and D.K. Robinson, Data reduction and error analysis for the physical sciences *McGraw-Hill Inc*, (1992).

[23] H. Anklin et al., *Nucl. Instr. and Methods in Phys. Res. A* **404**, 394 (1998).

[24] W. Grüebler et al., *Nucl. Phys. A* **334**, 365 (1980).

[25] S. Kovalski and H.A. Enge, Raytrace *MIT, Cambridge*, (1987).

[26] M. Laval et al., *Nucl. Instr. and Methods* **206**, 169 (1983).

[27] R. A. Cecil et al., *Nucl. Instr. and Methods* **161**, 439 (1979).

[28] J. E. Perry, Jr. and S. J. Bame, Jr., *Phys. Rev.* **99**, 1368 (1955).

[29] J. Carlson et al., *Nucl. Phys. A* **401**, 59 (1983).

[30] J. Jourdan et al., *Nucl. Phys. A* **453**, 220 (1986).

[31] H. Anklin et al., *Nucl. Phys. A* **636**, 189 (1998).

[32] H. Witała, *priv. comm.*, 2003.

[33] H. Akiyoshi et al., *Phys. Rev. C* **64**, 034001 (2001).

[34] S. Weinberg, *Phys. Lett. B* **251**, 288 (1990).

Curriculum Vitae

Personal data:

Name:	Tatiana Klechneva
Date of birth:	29. July 1974
Place of birth	St-Petersburg
Nationality:	Russia
Marital status:	married

Education:

1981 - 1991	school N518 in St-Petersburg
1991 - 1997	study at the St-Petersburg State Technical University
	field of specialization: Radiation safety of people and environment
	13. February 1997: Diploma Project on the theme "Photodetectors for the Endcap ECAL CMS (CERN) "

Scientific activity:

1997 - 1999	work at the Petersburg Nuclear Physics Institute in the Laboratory of Short-Lived Nuclei as a trainee
	field of activity: testing and investigation of the behavior of fine-mesh vacuum photodetectors (produced for CMS Endcap (CERN) in Russia) in a strong axial magnetic field,
	testing and energy-resolution measurements of BaF_2-crystals produced by the State Optical Institute (St-Petersburg) for the $\vec{d}p$-capture experiment, proposed by the group of Prof. I. Sick (University of Basel)
1999 - 2004	work at the Physical Institute of the University of Basel in the group of Prof. I. Sick as a PhD-student
	participation in the experiments performed by the group of Prof. I. Sick at the Paul Scherrer Institute ("Measurement of the neutron proton spin correlation parameter A_{zx}", "The tree-body break-up reaction") and at MAMI facility (Uni. Mainz) ("^{3}He-structure", "Measurement of the neutron electric form factor")
	participation in the Graduiertenkolleg Basel − Tübingen
17.February 2004	PhD-exam